



HAL
open science

Hybrid system combining mechanical compression and thermochemical storage of ammonia vapor for cold production

Jaume Fitó, Alberto Coronas, Sylvain Mauran, Nathalie Mazet, Maxime Perier-Muzet, Driss Stitou

► To cite this version:

Jaume Fitó, Alberto Coronas, Sylvain Mauran, Nathalie Mazet, Maxime Perier-Muzet, et al.. Hybrid system combining mechanical compression and thermochemical storage of ammonia vapor for cold production. *Energy Conversion and Management*, 2019, 180, pp.709 - 723. 10.1016/j.enconman.2018.11.019 . hal-02331028

HAL Id: hal-02331028

<https://hal.science/hal-02331028>

Submitted on 24 Oct 2019

HAL is a multi-disciplinary open access archive for the deposit and dissemination of scientific research documents, whether they are published or not. The documents may come from teaching and research institutions in France or abroad, or from public or private research centers.

L'archive ouverte pluridisciplinaire **HAL**, est destinée au dépôt et à la diffusion de documents scientifiques de niveau recherche, publiés ou non, émanant des établissements d'enseignement et de recherche français ou étrangers, des laboratoires publics ou privés.

1 Hybrid system combining mechanical compression and thermochemical storage 2 of ammonia vapor for cold production

3 Jaume Fitó^{a,b,c}, Alberto Coronas^c, Sylvain Mauran^{a,b}, Nathalie Mazet^a, Maxime Perier-Muzet^{a,b,*}, Driss Stitou^a

4 ^a CNRS-PROMES Laboratoire Procédés Matériaux et Energie Solaire UPR 8521, Perpignan 66100, France

5 ^b Université de Perpignan Via Domitia (UPVD), Perpignan 66860, France

6 ^c Department of Mechanical Engineering, Universitat Rovira i Virgili, Tarragona 43007, Spain

7 * Corresponding author. E-mail address: maxime.perier-muzet@univ-perp.fr.

8

9 A B S T R A C T

10 This paper studies a hybrid system for cold production consisting of a compression cycle combined with a thermochemical process
11 by sharing the same condenser, evaporator and refrigerant fluid. The aim of this hybridization is to solve mismatch issues between
12 the demand of cold and the source of energy (availability and/or price) with a system as compact as possible. One important side
13 benefit is that the interaction between the compressor and the thermochemical reactor reduces the activation temperature for
14 ammonia desorption in the thermochemical reactor. To study this interaction a quasi-steady simulation model for both storage
15 and de-storage phases has been developed and experimentally validated by means of a small scale (approx. 300 Wh of cold
16 storage) experimental bench with ammonia as refrigerant and barium chloride (BaCl_2) as reactant salt. Experiments proved a 35
17 K reduction in the activation temperature of the desorption reaction with respect to desorption without compressor. Model
18 validation by adjusting permeability and thermal conductivity of the reactive composite showed an acceptable agreement between
19 predicted and experimental reaction advancement-time curves. The validated model was used for simulation of the system in a
20 preliminary case study, representative in power (40 kW) and temperature (-25°C) of an industrial cold demand. It is shown that
21 during ammonia de-storage, the hybrid achieves a higher COP than a conventional mechanical vapor compression system. It
22 increases exponentially with the relative share of thermochemical storage in the cold production.

23 **Keywords:** Refrigeration, Hybrid system, Vapor compression refrigeration, Thermochemical storage, Low-grade heat source,
24 Heat and mass transfer.

25 H I G H L I G H T S

- 26 • Compression-thermochemical cooling system with electricity & low-grade heat input.
- 27 • 35 K heat source temperature reduction through compression-assisted desorption.
- 28 • Quasi-steady simulation model validated accounting for heat and mass transfers.
- 29 • Preliminary case study with bi-stage compression and cold production at -25°C .
- 30 • 2 times higher COP than vapor compression during ammonia de-storage phase.

Nomenclature

Names and variables

Greek symbols

G	Gas	Δ	Increment
h	Specific enthalpy, $kJ\cdot kg^{-1}$ or $kJ\cdot mol^{-1}$	ε	Fraction of cold produced by the thermochemical subsystem during synthesis phase
k	Permeability, m^2	η	Efficiency
M	Molar mass, $kg\cdot kmol^{-1}$	λ	Effective thermal conductivity, $W\cdot m^{-1}\cdot K^{-1}$
m	Mass, kg	μ	Dynamic viscosity, $Pa\cdot s$
\dot{m}	Mass flow rate, $kg\cdot s^{-1}$	ρ	Density, $kg\cdot m^{-3}$
\dot{n}	Mole flow rate, $mol\cdot s^{-1}$	$\bar{\rho}$	Apparent density, $kg\cdot m^{-3}$
P	Pressure, bar	τ	Compression ratio
\dot{Q}	Heat power, kW	ν	Reaction's stoichiometric coefficient, $mole\text{-}gas\cdot mole\text{-}salt^{-1}$
Q	Heat, kWh	ψ	COP ratio between hybrid system and MVC system
R	Thermochemical Reactor	ξ	Moles of refrigerant in the fully discharged salt
\mathfrak{R}	Ideal gas constant, $J\cdot mol^{-1}\cdot K^{-1}$		

r Radius, m

Subscripts and Superscripts

S	Solid	$^{\circ}$	Reference point
s	Specific entropy, $J\cdot kg^{-1}\cdot K^{-1}$ or $J\cdot mol^{-1}\cdot K^{-1}$	0	Fully discharged reactive salt ($X = 0$)
T	Temperature, $^{\circ}C$	1	Fully charged reactive salt ($X = 1$)
t	Time, h	c	Constraint temperature or pressure applied to the reactor
U_w	Global heat transfer coefficient, $W\cdot m^{-2}\cdot K^{-1}$	cd	Condenser
V	Volume, m^3	dec	Decomposition phase
\dot{V}	Volumetric flow rate, $m^3\cdot s^{-1}$	d	Gas diffuser
v	Specific volume, $m^3\cdot kg^{-1}$	ev	Evaporator
\dot{W}	Power, kW	eq	Equilibrium
W	Work, kWh	f1	Mass transfer-limited reaction front
w	Mass fraction, $kg\cdot kg^{-1}$	f2	Heat transfer-limited reaction front
X	Reaction advancement degree (-)	h	High temperature or pressure level
Z	Axial coordinate and length of reactive composite, m	HP	Relative to High-Pressure compressor

Acronyms

CAD	Compression-Assisted Decomposition	HYB	Hybrid system
COP	Coefficient Of Performance	i	Inlet
D#	Decomposition reaction experiment (# goes from 1 to 3)	l	Low temperature or pressure level
Dec	Energy storage density of the reactive composite, $kWh\text{-}heat / m^3\text{-}composite$ (based on heat of reaction)	LP	Relative to Low-Pressure compressor
ENG	Expanded Natural Graphite	m	Medium temperature or pressure level
EV	Expansion Valve	min	Minimum
HCTRS	Hybrid Compression-Thermochemical Refrigeration System	MVC	Mechanical Vapor Compression
		o	Outlet
		r	Reaction, reactor, or reactive composite

L/V	Liquid / Vapor	rd	Decomposition reaction
MVC	Mechanical Vapor Compression	rs	Synthesis reaction
MX	Metal halide	s	Isentropic
S#	Synthesis phase experiment (# goes from 1 to 3)	sa	Anhydrous reactive salt
TCH	Thermochemical	syn	Synthesis phase
TOD	Thermally-Only activated Decomposition	syn-dec	Complete TCH cycle (synthesis and decomposition)
V-XX	Valve number XX (goes from 01 to 16)	TCH	Thermochemical
		w	Reactor's wall

31 1. Introduction

32 The current need to reduce GHG emissions and decarbonize energy systems has increased the interest of using
 33 renewable sources and recovering low-grade waste heat in the recent decades [1]. The impact of cold production in
 34 the commercial sector is not negligible: for instance, supermarkets and hypermarkets represent 56 % of the total
 35 demand of cold in France's commercial sector [2]. Compression refrigeration is a mature technology, and if applied
 36 for solar operation, it can also benefit from the competitive costs of solar photovoltaic (PV) technology [3]. A classic
 37 problem is the mismatch between the solar resource and the cold demand [4,5]. If this mismatch is solved by having
 38 the system connected to the grid, it happens that the price of this source is variable, thus creating another type of
 39 mismatch (cold demand/source price). An answer to the problem of mismatch is energy storage, to store surplus cold
 40 during favorable periods (sunshine hours or low price of the source) for later use [6]. One idea is placing phase
 41 change materials (PCM) in the cold delivery unit, which has been studied experimentally for solar-PV compression
 42 refrigeration driven with DC motor [7]. Otherwise, the storage can be placed outside of the unit, as studied
 43 experimentally for solar-PV air conditioning with ice thermal storage [8], for instance, or the energy can be stored by
 44 means of batteries [9].

45 Thermochemical processes allow mid- and long-term energy storage with nearly negligible heat losses [10], for
 46 several applications such as solar air conditioning [11], cooling + heating [12], or long-term storage of solar energy
 47 [13]. Another interesting application proposed is deep-freezing [14], by means of a cascading process that has the
 48 added benefit of being driven by low-grade heat. Indeed, thermochemical systems can utilize low-grade to mid-grade
 49 heat sources depending on the choice of reactive pair [15], and usually, several useful effects can be obtained from
 50 these systems, such as cascaded use and storage of solar thermal energy [16], especially when they are configured
 51 with two reactive beds [17,18]. Several of the systems in these studies are ammonia-based [19]. The idea of replacing
 52 the condenser/evaporator with a secondary adsorbent reactor has also been investigated, under the name of
 53 resorption [20]. The notable advantages of thermochemical processes can make these processes economically

54 competitive in the near future. The idea of combining the maturity of vapor compression with the prospective
55 competitiveness of thermochemical storage seems promising.

56 The coupling of absorption or desorption processes with mechanical vapor expansion or compression was
57 patented by Moritz Honigmann in 1883 [21]. Recently, the so-called 'Honigmann process' was re-evaluated by
58 Jahnke et al. [22] as thermochemical storage producing power during desorption phase, and later simulated for the
59 LiBr/H₂O and NaOH/H₂O working pairs [23]. Bao et al. developed the idea of combining thermochemical processes
60 with vapor compression [24] and with vapor expansion [25]. The concepts were presented under the name of
61 'integrated chemisorption cycles', and the suggested applications were ultra-low grade (30 °C – 100 °C) heat recovery
62 and thermo-electric energy storage. The study considered ammonia as working fluid and manganese chloride
63 (MnCl₂), calcium chloride (CaCl₂) and sodium bromide (NaBr) as reactant salts. The coupling between the reactor
64 and the compressor is reported to show some instabilities because of the variable flow rate of ammonia entering the
65 compressor, and one solution proposed for similar systems (expansion/thermochemical) is to place a buffer tank at
66 the reactor outlet to reach constant inlet rate of ammonia [26,27]. Recently, Ferruci et al. [28] pursued the concept of
67 thermochemical storage driven by mechanical vapor compression activated by solar-PV energy. The system was
68 proposed with ammonia as refrigerant and barium chloride (BaCl₂) as reactant salt for cooling applications,
69 highlighting as main strengths the thermochemical storage and the possibility of using low-temperature heat sources
70 thanks to the compressor aiding the desorption of ammonia in the reactor.

71 Further studies on this hybrid thermochemical/compression system are not abundant, although several
72 experimental studies exist with thermochemical systems alone, especially with the NH₃/BaCl₂ reaction, and
73 mechanical vapor compression refrigeration is a mature technology. In addition, other concepts very similar to
74 hybridization have been proposed, for instance an adsorption/compression cascade system [29]. The idea of coupling
75 mechanical vapor compression with thermochemical storage can result in interesting hybrid systems with high
76 potential for waste heat utilization, and their experimental study is feasible.

77 This paper investigates further into this idea and studies experimentally an ammonia-based refrigeration system
78 consisting in the hybridization of compression refrigeration with thermochemical storage implementing the NH₃/BaCl₂
79 pair [30]. The main novelties of this paper with respect to literature are the approach chosen for simulation as well as
80 the experimental validation. The system utilizes low-grade heat thanks to its compression-assisted reduction of
81 activation temperature (described in Section 2), and benefits from the advantages of thermochemical storage. The
82 absorption, desorption, and compression-assisted desorption stages are simulated by means of a quasi-steady dual-
83 front model (Section 3). An experimental bench was built to validate the model by adjusting composite's permeability

84 and thermal conductivity, the most representative parameters of mass and heat transfer respectively (Section 4).
 85 Experimental results show a 35 K reduction in heat source temperature thanks to the compression-assisted
 86 desorption. The validated model is then used for simulation in a simplified case study (Section 5) of a different
 87 configuration of the hybrid system operating at different conditions with the $\text{NH}_3/\text{SrCl}_2$ and the $\text{NH}_3/\text{CaCl}_2$ pairs. This
 88 preliminary case study is offered for a permanent production of 40 kW cold at $-25\text{ }^\circ\text{C}$ which is representative of the
 89 needs for cold stores of supermarkets.

90 **2. System description**

91 Figure 1 depicts the operating principle of the hybrid compression-thermochemical refrigeration system (HCTRS)
 92 on a simplified Clausius-Clapeyron diagram. The vapor/liquid equilibrium of pure refrigerant is represented with a
 93 green line, and the red line represents a reversible solid/gas thermochemical reaction. The HCTRS consists of two
 94 subsystems: the mechanical vapor compression (MVC) subsystem, made up of a compressor, a condenser, an
 95 expansion valve and an evaporator; and the thermochemical (TCH) subsystem, made up of a thermochemical
 96 reactor, the condenser, a storage tank, the expansion valve and the evaporator. The hybridization consists of the
 97 same condenser, expansion valve, evaporator and refrigerant fluid being shared by both subsystems. The HCTRS
 98 requires an input of both electric and thermal energy and operates within 3 temperature levels and at least 2 pressure
 99 levels. Indeed, each subsystem can be operated separately from the other, but for the sake of simplicity, Fig. 1
 100 focuses only on the three most characteristic operating modes.

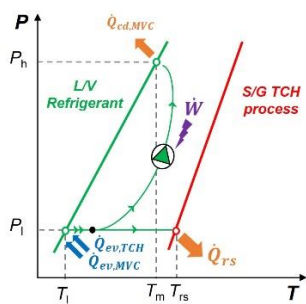


Fig. 1a: Simultaneous production of cold with the thermochemical subsystem (synthesis phase) and with the mechanical vapor compression subsystem, depicted in the Clausius-Clapeyron diagram.

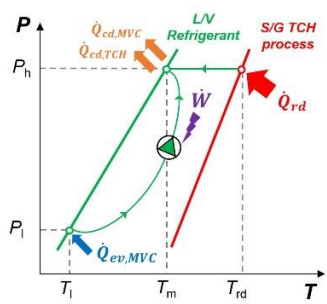


Fig. 1b: Cold production by the mechanical vapor compression subsystem with simultaneous storage of refrigerant by the thermochemical subsystem activated by thermal source only (classic decomposition phase) at condenser pressure.

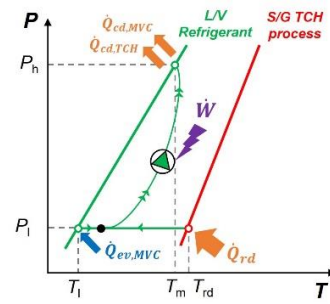


Fig. 1c: Cold production by mechanical vapor compression and simultaneous thermochemical storage of refrigerant activated by low-grade thermal energy at $P < P_h$, thanks to the compressor (compression-assisted decomposition).

101 The first one is simultaneous cold production by the MVC and the TCH (Fig. 1a). Stored refrigerant from the TCH
 102 is released into the evaporator and provides additional cold production. This can be used to assist the MVC in periods
 103 of peak demand with unstable electric source, or to reduce its load in the case of a stable electric source but with
 104 higher price. Thanks to the thermochemical process, the energy storage saves one step of energy conversion during
 105 the discharge stage, reducing the inertia of the system in comparison with electricity storage in batteries. Refrigerant
 106 vapor leaving the evaporator is divided into two streams: one enters the compressor for the MVC cycle, and the other
 107 reacts with the salt inside the TCH reactor, in an exothermic process with the reaction heat released at ambient
 108 temperature.

109 The second characteristic mode of the hybrid system is the possibility of producing cold by MVC while storing
 110 ammonia with the TCH activated with a heat source (Fig. 1b). Both ammonia streams leaving the compressor and
 111 the reactor join before entering the condenser. The part corresponding to TCH storage is kept in a tank right after
 112 condensing. This mode will be hereinafter called 'Thermally-Only activated Decomposition' (TOD) in this study. In
 113 TOD, activation temperatures can be relatively high depending on reactive pair and condenser pressure. This may
 114 force to discard certain heat sources that do not have enough temperature, as sometimes happens with classical
 115 TCH systems because of their monovariant equilibrium. Nevertheless, in the HCTRS the reactor and compressor
 116 can be connected to facilitate decomposition reactions at pressures lower than the condenser pressure, and therefore
 117 lower activation temperatures.

118 The third and most interesting operating mode, 'Compression-Assisted Decomposition' (CAD, Fig. 1c), makes
 119 this connection possible. The compressor allows the reactor pressure to be different from the condenser pressure,
 120 granting an additional degree of freedom. This allows decomposition at low pressure (P_l) simultaneously to MVC cold
 121 production. Of course, operating pressure can be adjusted to any value between P_l and P_h (it could be regarded as
 122 a 'floating' pressure level), to utilize any waste heat at the required temperature level for this suction pressure. This
 123 possibility can be investigated until process activation at ambient temperature: this case may well imply reactor
 124 pressures even lower than the low pressure level itself. The CAD enables low-grade waste heat recovery, as well as
 125 selection of well-performant reactive pairs (such as ammonia-barium chloride) despite heat source temperatures
 126 below reaction equilibrium temperature at condenser pressure.

127 The reversible solid/gas thermochemical reaction is usually written as in eq. (1). $\langle \text{MX} \rangle$ is a metallic salt reacting
 128 between ξ and $(\xi + \nu)$ moles of refrigerant gas (G), ν is the stoichiometric coefficient and Δh_r° is the standard enthalpy
 129 of reaction. The equilibrium formed by G, $\langle \text{MX} \cdot \xi \text{G} \rangle$ and $\langle \text{MX} \cdot (\xi + \nu) \text{G} \rangle$ is monovariant and represented by eq. (2),

130 where values of Δh_r^0 and Δs_r^0 referred by mole of gas (ammonia) are given by Touzain [31] for each reactive pair and
 131 assumed constant with respect to temperature. The reference pressure P^0 is 1 bar.

$$132 \quad \langle MX \cdot \xi G \rangle + \nu(G) \rightleftharpoons \langle MX \cdot (\xi + \nu)G \rangle + \nu \cdot \Delta h_r^0 \quad (1)$$

$$133 \quad \ln\left(\frac{P_{eq}}{P^0}\right) = \frac{-\Delta h_r^0}{\Re \cdot T_{eq,r}} + \frac{\Delta s_r^0}{\Re} \quad (2)$$

134 3. Modeling

135 The sizing of the two essential components of the HCTRS hybrid system, namely the compressor and the reactor,
 136 depends mainly on the temperatures of the heat sources and sinks (in particular the one to which the cold is
 137 delivered), the desired cooling power and the scenario of storage and restitution, i.e. the energies and respective
 138 powers provided by the two subsystems MCV and TCH. For common applications, such as the one discussed in
 139 Section 5, the sizing of the compressor is straightforward (issue from suppliers' catalogs). It must be able to aspirate
 140 the sum of both ammonia flow rates coming from evaporator and reactor in CAD phase.

141 On the other hand, the design of the reactor is not so obvious. Indeed the running of the solid / gas reactor is
 142 intrinsically unsteady, with instantaneous power decreasing overall between the beginning and the end of the
 143 reaction, both in synthesis and in decomposition phases, and even when the thermodynamic constraints (T and P)
 144 applied to the reactor are kept stable. The modeling of this hybrid system is therefore more complex, and even more
 145 so when the reactor is coupled to the compressor during the CAD phases, given the antagonistic contributions of the
 146 compressor and the reactor that affect the reactor pressure: the decomposition reaction releases refrigerant gas
 147 (thus contributing to pressure increase) while the compressor removes it (thus contributing to pressure decrease).

148 In all cases, including purely thermal decompositions (TOD), reactor modeling is necessary to estimate the
 149 performance of HCTRS systems with different solid / gas reactions, thermodynamic constraints and reactor sizes.
 150 This modeling, detailed below, allowed to firstly dimension an experimental bench of a HCTRS system with a small
 151 power, and secondly to fit with sufficient precision the parameters of the model on a whole series of experiments.

152 3.1. Model's hypotheses

153 There are several more or less sophisticated models able to describe solid / gas reaction rate as a function of the
 154 implementation of the reagent, the applied thermodynamic constraints (T_c , P_c) and the geometry of the inner heat
 155 exchanger and gas diffuser. The most accurate [32] is based on the resolution of a system coupling the equation of
 156 heat and that of mass conservation, including the terms of accumulation (i.e. sensible heat and variation of mass of

157 gas in the porous volume). In this model, the gas flow rates and the reaction heat fluxes are connected by a kinetic
 158 law of transformation of the reactive grain, which is a function of a local deviation from the thermodynamic equilibrium.
 159 On the other hand, the simplest model [33] assumes a uniform and constant temperature of the reactant during the
 160 reaction and a reaction rate solely as a function of an overall coefficient of heat exchange between the reactive solid
 161 and the coolant. The model used here is of intermediate complexity; it neglects the terms of accumulation and
 162 therefore does not adequately reflect evolutions in the temperature and pressure profiles within the reactive fixed
 163 bed. On the other hand, it correctly accounts for reactor power evolutions that are more useful for quantifying the
 164 performance of an HCTRS system.

165 The model is constructed for a reactive medium with a cylindrical geometry (Fig. 2) and calculations are carried
 166 out in the radial direction. Refrigerant gas (assumed as a perfect gas) at the constraint pressure P_c leaves or enters
 167 the cylindrical reactor through a gas diffuser in its axis, and the constraint temperature T_c is applied via a heat transfer
 168 fluid circulating through an external coil exchanger at the peripheral wall. The advancement degree of the reaction is
 169 bound to limitations of heat transfer and mass transfer, and the model takes both into account.

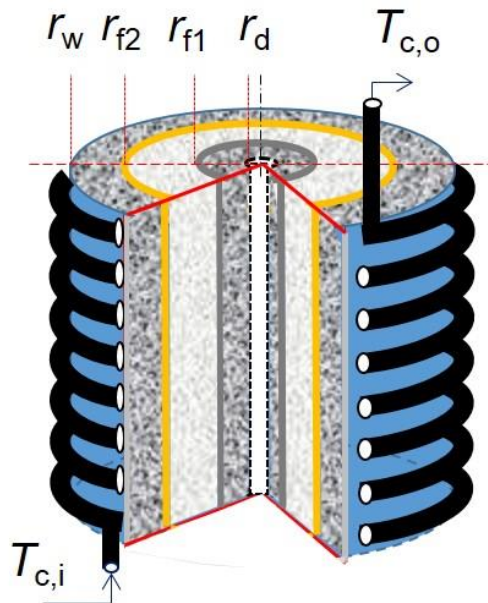


Fig. 2: Schematic view of the thermochemical reactor. During synthesis, dark grey area represents salt that already reacted and light grey area corresponds to salt that is yet to react, and vice versa during decomposition phase. The yellow (at r_{f2}) and grey (at r_{f1}) boundaries are the two fronts of reaction.

The main hypothesis of this model (also detailed in [32,34]) is the existence of two ‘sharp’ reactive fronts, after named by simplicity: the “heat front” (identified by the index f2 and located at the radius r_2 in Fig. 2), based on a purely heat transfer limiting case, moving from the reactor wall (r_w) to the gas diffuser (r_d), and the “mass front” (identified by the index f1 and located at the radius r_1 in Fig. 2), based on a purely mass transfer limiting case, moving from the gas diffuser to the reactor wall. From a cross-section view of the solid reactive medium, two areas can be distinguished at an intermediate time of the reaction: in synthesis phase, the dark grey area represents the reactive medium that has fully reacted (i.e. at $X = 1$) and the light grey area represents the one that is yet to react (i.e. at $X = 0$), and vice versa in decomposition phase. The reaction ends when reactive fronts finally meet each other, which happens at a radial position that depends on experiment conditions. Main model hypotheses are:

- Heat transfer and mass transfer are the two limiting phenomena, while reaction kinetics is not. So on the two reaction fronts the local temperature and pressure couples (T_{f1}, P_{f1}) and (T_{f2}, P_{f2}) correspond to the thermodynamic equilibrium (eq. 3) and heat power and mass flow given by the reaction are function of the heat and mass transfer properties of the fixed bed on one hand, and on the other hand of the temperature drop and pressure drop between these fronts and the exchanger wall and gas diffuser respectively and between the two fronts also.
- Composite properties and conditions (pressure, temperature) are uniform along the axial direction.
- Convective heat transfer between refrigerant gas and reactive composite is neglected.
- Accumulation terms are neglected (sensible heat and accumulation of refrigerant gas within the porous volume of the reactive).
- Pseudo-steady state is assumed between the two successive advancements of reaction (X and $X + \Delta X$), therefore T , P and dX/dt (rate of reaction) do not vary in this interval.

3.2. Model's governing equations

Some of the following equations are available for the decomposition reactions (equations noted #d); those of synthesis (equations noted #s) are similar with in particular an inversion of the heat and mass transfer coefficients between the reactive medium that have fully reacted and the un-reacted one (see below).

$$\ln\left(\frac{P_{f\#}(t)}{P^o}\right) = -\frac{\Delta h_r^o}{\mathfrak{R} \cdot T_{f\#}(t)} + \frac{\Delta S_r^o}{\mathfrak{R}} \quad \{\# = 1,2\} \quad (3)$$

195 Conventionally the global advancement X evolves between 1 and 0 for a decomposition reaction. It is linked by
 196 (4d) to the partial advancements X_{f1} and X_{f2} , which are themselves function of the radial position of the two fronts
 197 (5d, 6d).

$$198 \quad X(t) = (X_{f1}(t) + X_{f2}(t)) - 1 = X(t - 1) - \Delta X \quad (4d)$$

$$199 \quad X_{f1}(t) = 1 - \frac{r_{f1}^2(t) - r_d^2}{r_w^2 - r_d^2} \quad (5d)$$

$$200 \quad X_{f2}(t) = 1 - \frac{r_w^2 - r_{f2}^2(t)}{r_w^2 - r_d^2} \quad (6d)$$

201 At each simulation step, the new X is calculated from the previous one with the selected step ΔX (4d). The
 202 advancement degrees related to the progression of the heat and mass fronts are calculated by means of the individual
 203 and global speeds of reaction (by deriving eq. 4d), and the global reaction rate is the sum of the reaction rates of
 204 both fronts. The gas flows and heat powers within the reactive fixed bed are deduced respectively from the application
 205 of Darcy's law and Fourier's law. In addition, the gas flows and heat powers are coupled via the enthalpy of reaction
 206 or alternatively via the energy density of the reactive composite (eq. 7).

$$207 \quad \dot{Q}_{\#}(t) = \dot{n}_{\#}(t) \cdot \Delta h_r^{\circ} = n_s \cdot v \cdot \frac{dX_{\#}}{dt}(t) \cdot \Delta h_r^{\circ} = [Dec \cdot \pi \cdot Z \cdot (r_w^2 - r_d^2)] \cdot \frac{dX_{\#}}{dt}(t) \quad \{\# = f1, f2, \text{ or no subscript} \} \quad (7)$$

208 The spatial integration of the Darcy and Fourier equations in radial unidirectional transfers and steady state is
 209 done for:

210 - the total molar gas flow $\dot{n}(t)$ between the boundaries r_{f1} and r_d (eq. 8d);

211 - the molar flow of gas $\dot{n}_{f2}(t)$ desorbed by the so-called "heat front" between boundaries r_{f2} and r_{f1} (eq. 9d) ;

212 - the total heat power $\dot{Q}(t)$ between the boundaries r_w and r_{f2} (eq. 10d);

213 - the heat power $\dot{Q}_{f1}(t)$ absorbed by the so-called "mass front" between the boundaries r_{f2} and r_{f1} (eq. 11d).

$$214 \quad \frac{\dot{n}(t) \cdot \mathfrak{R} \cdot T_c}{2\pi \cdot Z} = [Dec \cdot (r_w^2 - r_d^2)] \cdot \frac{dX}{dt}(t) \cdot \frac{\mathfrak{R} \cdot T_c}{2 \cdot \Delta h_r^{\circ}} = \left\{ \frac{k_0}{2 \cdot \mu} [P_c^2 - P_{f1}^2(t)] \right\} / \ln \left[\frac{r_{f1}(t)}{r_d} \right] \quad (8d)$$

$$215 \quad \frac{\dot{n}_{f2}(t) \cdot \mathfrak{R} \cdot T_c}{2\pi \cdot Z} = [Dec \cdot (r_w^2 - r_d^2)] \cdot \frac{dX_{f2}}{dt}(t) \cdot \frac{\mathfrak{R} \cdot T_c}{2 \cdot \Delta h_r^{\circ}} = \left\{ \frac{k_1}{2 \cdot \mu} [P_{f1}^2(t) - P_{f2}^2(t)] \right\} / \ln \left[\frac{r_{f2}(t)}{r_{f1}(t)} \right] \quad (9d)$$

$$216 \quad \frac{\dot{Q}(t)}{2\pi \cdot Z} = Dec \cdot (r_w^2 - r_d^2) \cdot \frac{dX}{dt}(t) \cdot \frac{\mathfrak{R} \cdot T_c}{2} = \left\{ \lambda_0 \cdot [T_{f2}(t) - T_w(t)] \right\} / \ln \left[\frac{r_w}{r_{f2}(t)} \right] = r_w \cdot U_{w0} \cdot [T_w(t) - T_c] \quad (10d)$$

$$217 \quad \frac{\dot{Q}_{f1}(t)}{2\pi \cdot Z} = [Dec \cdot (r_w^2 - r_d^2)] \cdot \frac{dX_{f1}}{dt}(t) \cdot \frac{R \cdot T_c}{2} = \{\lambda_1 \cdot [T_{f1}(t) - T_{f2}(t)]\} / \ln \left[\frac{r_{f2}(t)}{r_{f1}(t)} \right] \quad (11d)$$

218 Where k_0 , k_1 are the permeability of the fixed layers respectively at $X = 0$ and $X = 1$, λ_0 , λ_1 are the conductivities of
 219 the same fixed layers and Uw_0 a global heat transfer between the heat transfer fluid and the reactive salt (also at
 220 $X=0$ from the beginning of the decomposition) at the inner boundary of the heat exchanger wall of the reactor which
 221 involves the temperature T_w (variable during the reaction) at this interface. D_{ec} is the energy density refer to the heat
 222 of reaction and the apparent volume of the reactive composite \tilde{V}_c and it is linked to two other implementation
 223 parameters (eq. 12): the mass fraction of anhydrous salt (w_{sa}) and the apparent density of expanded natural graphite
 224 ($\tilde{\rho}_{ENG}$). Indeed, the reactive salt is mixed with expanded natural graphite (ENG) because this binder, which is
 225 chemically inert, makes it possible to obtain a reactive, porous and consolidated composite having much better heat
 226 transfer properties than a simple fixed bed consisting of salt alone [35], and hence a better specific power of the
 227 reactor. The high porosity of ENG leaves plenty of empty space within the reactive bed. When the grains of barium
 228 chloride react with ammonia and swell up, this empty space prevents agglomeration and ensures that the contact
 229 surface between the salt and the ammonia is always sufficient.

230 Consequently for the implementation of the composite there are two degrees of freedom since the mass ratio of
 231 anhydrous salt (w_{sa}) and the final volume of the composite can be controlled in a wide range (unlike what is possible
 232 with salt alone). The values, given in Table 2 (next section), of the two implementation parameters chosen, w_{sa} and
 233 $\tilde{\rho}_{ENG}$ (this last one being the ratio between mass of binder and apparent volume of composite) correspond to a
 234 compromise between the specific reactor power and its energy density D_{ec} , the latter parameter being a function of
 235 the other two.

$$236 \quad Dec = \frac{n_s \cdot v \cdot \Delta h_r^\circ}{\tilde{V}_c} = \frac{w_{sa}}{1-w_{sa}} \cdot \tilde{\rho}_{ENG} \cdot \frac{v \cdot \Delta h_r^\circ}{M_{sa}} \quad (12)$$

237 For the reaction of synthesis the global advancement X evolves now between 0 and 1, so:

$$238 \quad X(t) = (X_{f1}(t) + X_{f2}(t)) = X(t-1) + \Delta X \quad (4s)$$

$$239 \quad X_{f1}(t) = \frac{r_{f1}^2(t) - r_d^2}{r_w^2 - r_d^2} \quad (5s)$$

$$240 \quad X_{f2}(t) = \frac{r_w^2 - r_{f2}^2(t)}{r_w^2 - r_d^2} \quad (6s)$$

241 The equations (8d) to (11d) relating to the decompositions become respectively the equation (8s) to (11s) relating
 242 to the synthesis by changing in the first ones the transfer parameters k_0 , k_1 , λ_0 , λ_1 and Uw_0 with respectively the
 243 parameters k_1 , k_0 , λ_1 , λ_0 and Uw_1 .

244 In the equations (8d) to (11d) and (8s) to (11s) the thermodynamic constraints T_c and P_c are written as constant,
 245 but they may be variable. In that case (encountered with the experimental study below) the values $T_c(t)$ and $P_c(t)$
 246 must be included in the code as boundaries conditions.

247 At each iteration the variables T_{f1} , P_{f1} , P_{f2} , $\frac{dX_{f1}}{dt}$, $\frac{dX_{f2}}{dt}$, T_w , etc. are determined from the system of equations (3) to
 248 (11d) or (3) to (11s) and the variable T_{f2} is calculated by the Newton-Raphson iterative method.

249 4. Experimental study

250 An experimental study was carried out on a HCTRS system of rather small power, but nevertheless
 251 representative of the physical phenomena that would be involved in a case of realistic application (treated in section
 252 5). The main objectives of this study were:

- 253 • To verify that the temperature reduction of the source heat is feasible.
- 254 • To obtain reaction's advancement degree as a function of time ($X-t$ curves) of three synthesis and two
 255 TODs at different operating conditions.
- 256 • To obtain the $X-t$ curve of a CAD at low constraint pressure.
- 257 • To validate the quasi-steady simulation model by adjusting parameters related to heat and mass transfer,
 258 i.e. permeability and thermal conductivity of both charged and discharged reactive composite and global
 259 heat transfer coefficient from reactive composite to heat exchange fluid.
- 260 • To register temperature and pressure evolutions within the reactive composite for qualitative discussion
 261 about their mutual influence.

262 The chosen salt was barium chloride (Fig. 3), because its low activation temperature makes it adequate for low-
 263 grade heat sources. Nevertheless, another two salts, calcium chloride and strontium chloride, are also suitable for
 264 such applications and were taken into account for the case study presented later in this paper.

265 The experimental setup (Fig. 4 and 5) was designed in collaboration between the CREVER Group (Spain) and
 266 the PROMES laboratory (France) [30]. It is made up of one thermochemical reactor, one electrically driven vapor
 267 compressor, one storage tank with level probe, two flat plate heat exchangers as condenser and evaporator, one

268 expansion valve, three thermal baths, a set of temperature and pressure measurement devices, and several process
 269 valves.

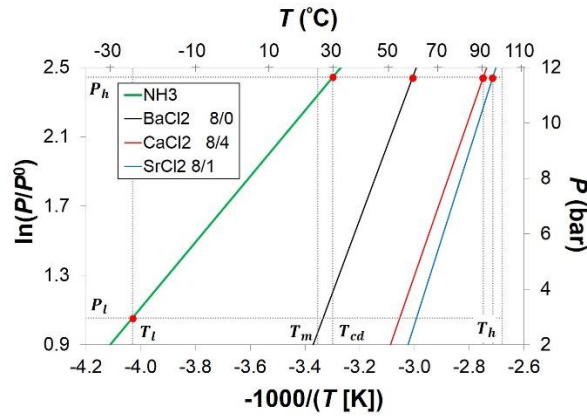


Fig. 3: Thermodynamic equilibrium of pure ammonia and selected solid/gas thermochemical reaction pairs with their ξ and ν stoichiometric coefficients ($\text{BaCl}_2 \cdot 0\text{-}8\text{NH}_3$, $\text{CaCl}_2 \cdot 4\text{-}8\text{NH}_3$ and $\text{SrCl}_2 \cdot 1\text{-}8\text{NH}_3$), represented on the Clausius-Clapeyron diagram. Operating conditions of the case study are also included.

270

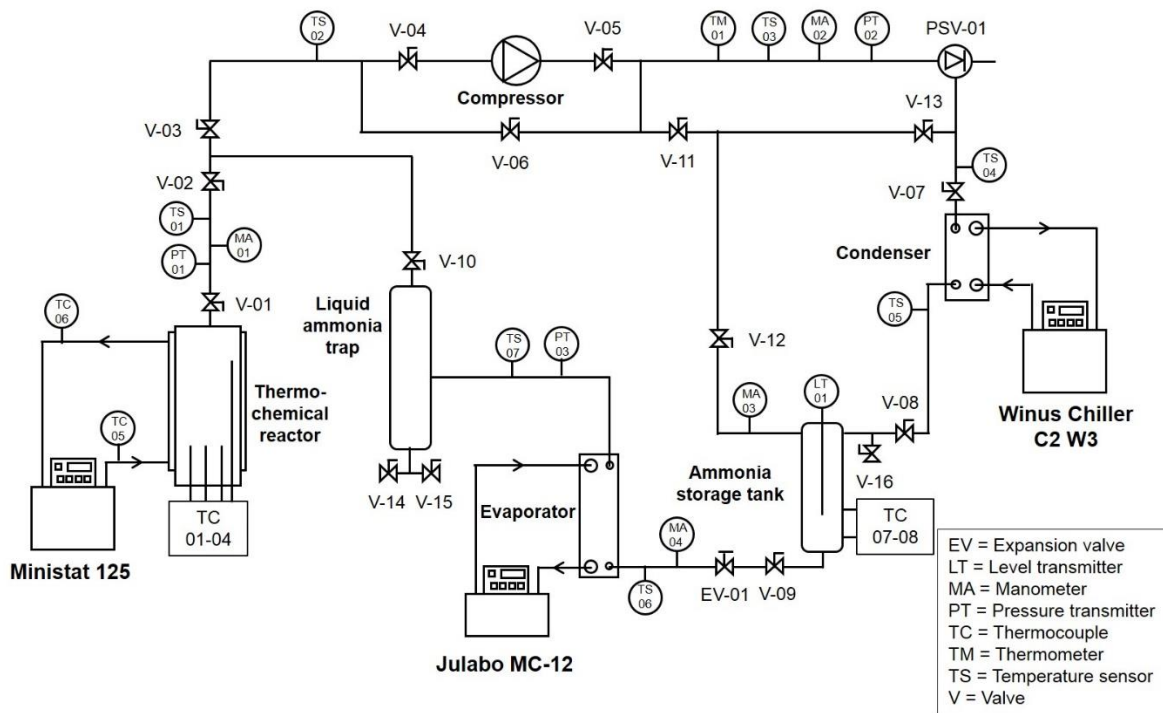


Fig. 4: Flow diagram of the setup used for experimental study of the hybrid compression-thermochemical refrigeration system. Main components, valves and measurement devices are represented.

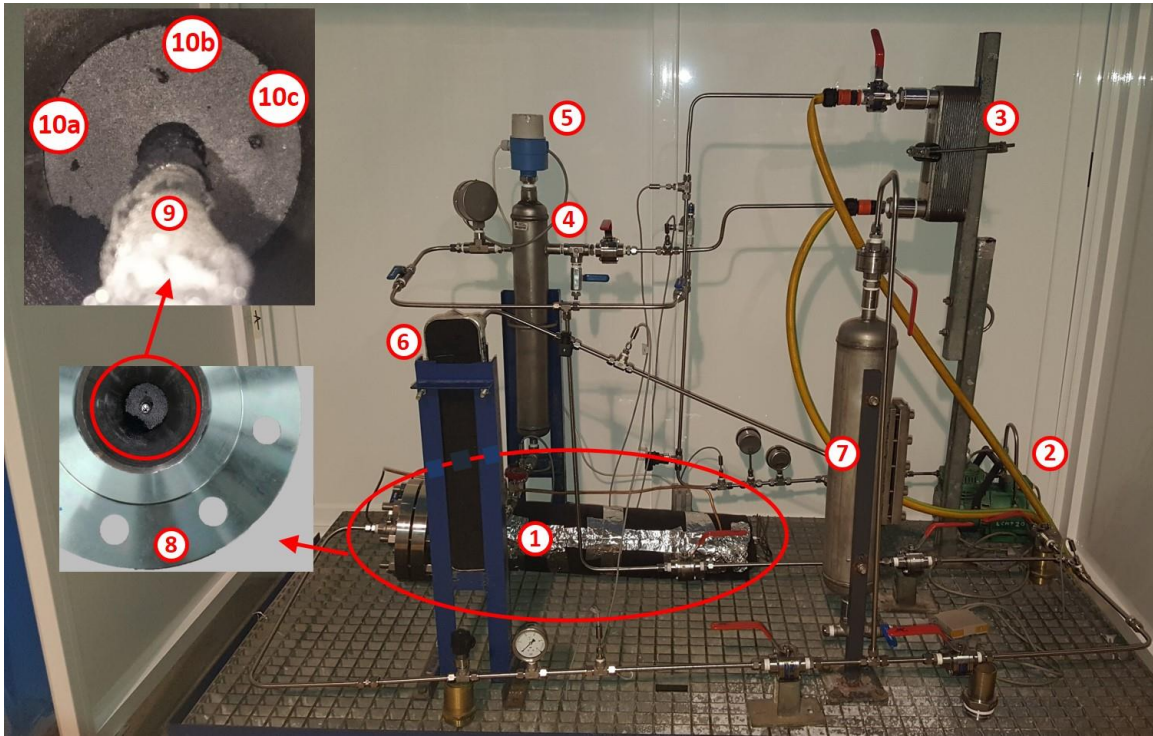


Fig. 5: Picture of the setup (before thermal insulation) used for experimental study of the hybrid compression-thermochemical refrigeration system. The main components are identified with labels. Two additional pictures are also embedded: one front view of the thermochemical reactor (flange open) that shows the reactive composite in the inside, and a zoomed picture showing radial position of 3 of the 4 thermocouples placed inside the composite. List of items: 1) Reactor; 2) Compressor; 3) Condenser; 4) Storage tank; 5) Level probe; 6) Evaporator; 7) Liquid trap; 8) Reactor's flange; 9) Reactor's internal gas diffuser; 10) Reactor's internal thermocouples at different radial positions.

271

272 The thermochemical reactor is cylindrical and made out of stainless steel 316. The upper end is flat and closed
 273 with a flange and EPDM flat sealing. The bottom is also flat and has four perforations for thermocouples TC01-04.
 274 Inside the reactor there is a in-situ compressed composite made up of $BaCl_2$ salt mixed with expanded natural
 275 graphite (ENG), an inert enhancer for heat and mass transfer. The preparation of this composite and its charge into
 276 the reactor is a specialized procedure from the Promes laboratory, and further description is available in [30]. The
 277 reactor also has an external thermal jacket consisting of a copper tube rolled around the external wall and surrounded
 278 with a high conductivity thermal paste. Type T thermocouples were used at the inlet (TC-05) and outlet (TC-06) of
 279 the heat transfer fluid from the reactor's thermal jacket. Relevant data about the reactor and the experimental bench
 280 are collected in Tables 1 and 2.

281

282

283 Table 1: Relevant data of the experimental bench: dimensions of the thermochemical reactor and reactive composite, intensive parameters of
 284 implementation of the solid reactive composite, and final values of the heat and mass transfers parameters after model validation.

Extensive parameters for reactive solid implementation							
r_d	r_{Tr-02}	r_w	Z	m_{sa}	m_{ENG}	m_{NH_3} reacting	Q_{ev}
m				kg			Wh cold
0.005	0.045	0.055	0.6	1.316	0.536	0.865	300
Intensive parameters				Heat and mass transfers			
w_{sa}	$\tilde{\rho}_{ENG}$	Dec	$k_0 = k_1$	$\lambda_0 = \lambda_1$	$Uw_0 = Uw_1$		
-	kg/m ³	kWh/m ³	m ²	W/(m·K)	W/(m ² ·K)		
0.71	100	100	10 ⁻¹⁴	1.4	170		

285

286 Three thermal baths are connected to the setup through external connections. The bath connected to the reactor's
 287 thermal jacket has a maximum heating power of 1 kW at a maximum delivery temperature of 150 °C, and a maximum
 288 cooling power of 0.3 kW at 20 °C. The bath connected to the evaporator provides heating with a maximum power of
 289 1 kW, and the bath connected to the condenser provides cooling with a maximum power of 1.5 kW. Two SS316 flat
 290 plate heat exchangers were used in counter-flow as condenser and evaporator. Several temperature and pressure
 291 measurement devices were placed throughout the setup, for monitoring purposes. Measurements were recorded
 292 with a data acquisition unit consisting of an Agilent® 34901A data logger with two 20-channel (2/4-wire) Keysight®
 293 multiplexer modules. Further information is available in [30].

294 The most important information derived from experiences is the advancement degree (X) vs time (t) curve of
 295 reaction. X - t curves indicate whether or not full reaction is achieved and within how much time. In this study, these
 296 curves were derived from the mass of ammonia inside the solid composite, which was calculated from indirect
 297 measurements. A capacitive probe (named LT01 in figure 4) was placed inside the storage tank to measure the level
 298 of liquid ammonia, and this level was converted to mass knowing the density (derived from temperature readings
 299 from TC07-08). This calculation assumes that during reaction, all ammonia entering the tank comes from to the
 300 reactor, or vice versa. Thermocouples TC01-04 were relevant for registering temperature evolutions inside the
 301 composite. The CAD is the main focus of this experimental study, although the setup allows bypassing the
 302 compressor (V-04 and V-05 closed, V-06 open) to carry out the TOD.

303 A set of experiments (Table 2) was designed within a certain range of activation temperatures T_c and operating
 304 pressures P_c . The equilibrium drop (ΔT_{eq}) is defined as the difference between the reaction's equilibrium temperature
 305 at the given operating pressure, and the average temperature of the heat exchange fluid. It influences implicitly the
 306 speed of the process (see equations 10d or 10s above).

Table 2. List of experiments used for model validation, including the type of reaction, operating conditions and valves configuration. Valves not mentioned are supposed to be permanently closed.

Experiment code	S1	S2	S3	D1	D2	D3
Reaction	$\langle BaCl_2 \rangle + 8(NH_3)$ $\rightarrow \langle BaCl_2 \cdot 8NH_3 \rangle$			$\langle BaCl_2 \cdot 8NH_3 \rangle \rightarrow \langle BaCl_2 \rangle + 8(NH_3)$		
Type of reaction	Synthesis			TOD		CAD
Open valves (Fig. 4)	V01-02, V09-10, EV-01			V01-03, V06-08, V11-13		V01-05, V07-08, V11-13
P_c [bar]	3.45	3.57	5.10	5.0	7.2	0.6
$T_{c,avg}$ [°C]	9.8	11.7	11.8	78.9	65.8	19.4
ΔT_{eq} [°C]	-19.9	-18.5	-25.7	41.8	20.8	25.6

307

308 Model validation was done by comparing experimental $X-t$ curves with model predictions after parameter
 309 adjustment. The validation consisted of adjusting the values of parameters λ_0 , λ_1 , k_0 , k_1 , Uw_0 and Uw_1 by the least
 310 squares method in an iterative procedure. As shown in Table 1, adjusted values were $\lambda_0 = \lambda_1 = 1.4 \text{ W}\cdot\text{m}^{-1}\cdot\text{K}^{-1}$, $k_0 = k_1$
 311 $= 10^{-14} \text{ m}^2$ and $Uw_0 = Uw_1 = 170 \text{ W}\cdot\text{m}^{-2}\cdot\text{K}^{-1}$. In practice the pairs of values $[\lambda_0, \lambda_1]$, $[k_0, k_1]$ and $[Uw_0, Uw_1]$ can differ
 312 slightly, but they were finally assumed equal for the sake of simplicity. Thus the validation of the model on all the
 313 experiments is done by adjustment of only three parameters.

314 Figure 6 shows data confrontation for experiments D1-D3, where each experiment is distinguished by one color.
 315 Continuous lines represent experimental curves, while dashed lines represent predictions after parameter
 316 adjustment. As expected, the advancement degree (X) evolves from 1 to nearly 0 throughout the reaction and in all
 317 cases the process is faster at the beginning than at the end. In the case of the TODs, it is observed that a higher
 318 equilibrium drop results in lower reaction times, which is logical.

319 Predicted reaction times are overestimated for D1 (TOD) and underestimated for D2 (TOD) and D3 (CAD), which
 320 could be regarded as a sign that there is no systematic bias in model predictions. Predicted curves are relatively
 321 close to experimental ones, and maximum deviations are observed towards the end of the process. A slightly more
 322 accurate adjustment might be possible with independent values of λ_0 and λ_1 as well as k_0 and k_1 . At the first stages
 323 of a decomposition λ_1 and k_1 are dominant, while λ_0 and k_0 gain weight towards the end, exactly where the highest

324 deviations are observed. Lower values of λ_0 or k_0 would increase the values of predicted times, leading to better curve
 325 fitting for D2 and D3, but higher deviations in D1.

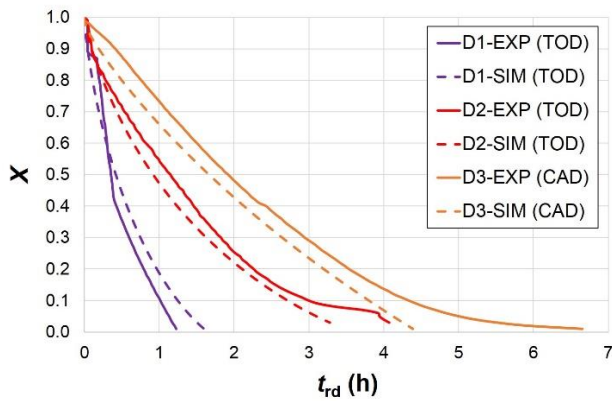


Fig. 6: Results of model validation: confrontation of experimental and simulated $X-t$ curves for the three decomposition reactions used for validation (two TODs and one CAD). Operating conditions and other data available in Tables 1 and 2.

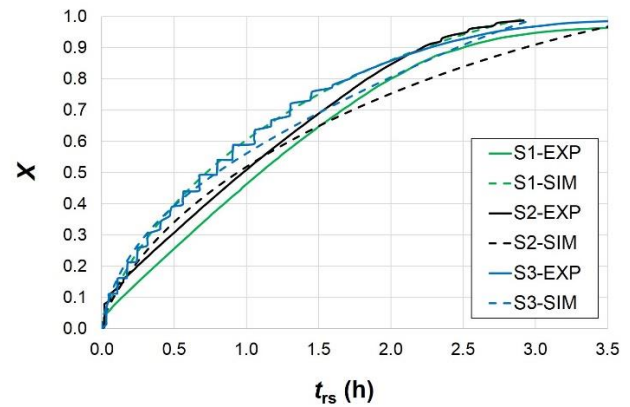


Fig. 7: Results of model validation: confrontation of experimental and simulated $X-t$ curves for the three synthesis reactions used for validation. Operating conditions and other data available in Tables 1 and 2.

326

327 Orange lines show data confrontation for experiment D3 (CAD). At first glance, it is observed that predictions fit
 328 most of the experimental data acceptably, except for the final reaction time. This deviation is probably caused by the
 329 low constraint pressure (around 0.6 bar) throughout the experiment, in comparison with the other experiments. At
 330 such low pressure, mass transfer limitations become non-negligible and slow the reaction down. This would also
 331 explain why the actual reaction is generally slower than the prediction, and why D3 is slower than D2 despite having
 332 a higher equilibrium drop (25.6 °C in front of 20.8 °C in D2, see Table 1). Also, D1 and D3 have similar equilibrium
 333 drops but the heat source temperature in D3 is much lower, which is taken as a proof that the activation temperature
 334 has been lowered thanks to the compressor-reactor coupling.

335 Predictions for syntheses (Fig. 7) are acceptable. The best fitting is observed for synthesis S3 (blue lines),
 336 although the model overestimates reaction times until almost the end of reaction, where it underestimates end
 337 reaction time. In the case of S1, the model consistently underestimates reaction times, while for S2 there seems to
 338 be a noticeable change in slope mid-reaction.

339 For the conditions of this study, the model predicts the $X-t$ curves of TOD, CAD and synthesis with less than 20
 340 % average deviation in reaction times within the realistic domain of operation (i.e. $0.05 < X < 0.95$). Given the
 341 simplifications in this model, such accuracy was considered sufficient for validation. A tendency is observed in which
 342 the model slightly overestimates final reaction times in the fastest reactions, and underestimates them in the slowest

343 reactions. Further, better accuracy can probably be reached with a more detailed, calculation-intensive adjustment
 344 method, although such procedure is out of the scope of this study.

345 Temperature and pressure measurements lead to some interesting evolutions for qualitative discussion, collected
 346 in Figure 8. This figure shows the evolutions of reactor's temperature and pressure, heat exchange fluid's inlet and
 347 outlet temperatures, and equilibrium temperature of reaction at reactor pressure in two experiments: a) Synthesis
 348 S2; b) CAD D3.

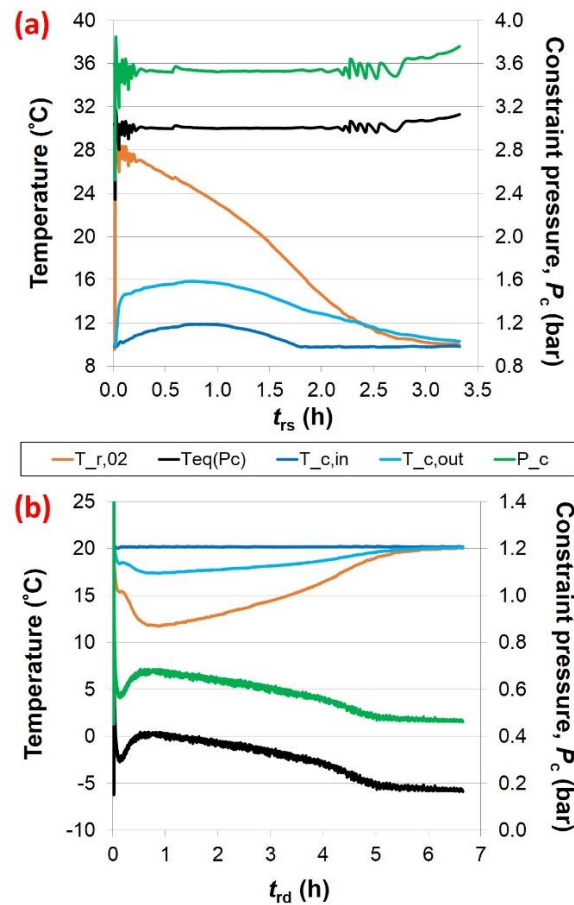


Fig. 8: Evolution, throughout reaction progress, of operating pressure, equilibrium temperature of the thermochemical reaction at the operating pressure, internal temperature of the solid reactive composite, and inlet and outlet temperatures of the heat exchange fluid, for: (a) synthesis S2; (b) CAD D3.

349 In Fig. 8a, variables show typical evolutions for a synthesis reaction. At the precise moment where the constraint
 350 pressure is applied by opening the valve V-01 (see Fig.4), the temperature of the reactive composite (" $T_{r,02}$ ", orange
 351 line) rises suddenly to almost the equilibrium temperature of reaction (" $T_{eq}(P_c)$ ", black line) at this given operating

352 pressure (“ P_c ”, green line). This happens because heat of reaction is released too quickly for the heat exchange fluid
 353 to evacuate it. This step is called by language abuse, the adiabatic phase of the reaction. Shortly after, temperatures
 354 within the solid composite start to descend, and as the reaction becomes slower, they get closer to T_c . When $T_{r,02} =$
 355 T_c , reaction end is reached and all reaction heat has been evacuated. The change in both the inlet and outlet heat
 356 transfer fluid temperatures (“ $T_{c,in}$ ”, dark blue, and “ $T_{c,out}$ ”, light blue) during reaction progress is noticeable. These
 357 temperatures rise during approximately the first third of reaction, then reach a maximum, and start decaying until end
 358 of reaction. This is a sign that the thermal bath connected to the reactor’s thermal jacket was limiting during synthesis
 359 reactions, which is in agreement with the straight slopes seen at the $X-t$ curves of experiments S1-S3 (Fig. 7).

360 In Fig. 8b, same variables and color code are kept from Fig. 8a. Nevertheless, variables show typical evolutions
 361 for a decomposition reaction: $T_{r,02}$ drops noticeably at the beginning (similar phenomenon as in synthesis, but in
 362 opposite sense) and rises back slowly until equaling T_c by the end of reaction. This time, however, the thermal bath
 363 was not limiting (it was the same bath as in synthesis but in heating mode): $T_{c,out}$ dropped just very slightly and, more
 364 importantly, $T_{c,in}$ remained stable at target value. Thus, T_c can almost be considered constant in this experience.

365 The most interesting evolution in Fig. 8b is the constraint pressure (P_c). As discussed in the description of the
 366 dual-front simulation model (Section 3.1), the ‘mutual constraint’ between compressor and thermochemical reaction
 367 has an influence on operating pressure, which should be variable and strictly decreasing throughout compression-
 368 assisted decomposition. Its evolution in experiment D3 (CAD) reflects this discussion perfectly. From $t_{rd} = 0.5$ h to t_{rd}
 369 $= 5$ h, P_c falls gradually from 0.7 bar to 0.45 bar, which reflects the competition between the compressor and the
 370 decaying reaction kinetics. By the end of reaction, operating pressure stagnates at a value that was identified as the
 371 compressor’s minimum suction pressure for the maximum compression ratio of 8 (given by the manufacturer) with
 372 the given discharge pressure (condenser pressure, which was 3.5 bar).

373 Although the original dual-front reaction model considers that T_c is constant and uniform, in practice the
 374 differences between $T_{c,in}$ and $T_{c,out}$ and their variations with time forced the implementation of variable profiles of T_c
 375 $= f(t)$ in the model for validation. This was especially necessary for synthesis reactions. This was done by means of
 376 a function adjusted from experimental mean temperature between $T_{c,in}$ and $T_{c,out}$ at every measurement. A similar
 377 approach was used for P_c during CAD: the compressor/reactor interaction caused this pressure to be variable, so P_c
 378 $= f(t)$ functions were implemented in the simulations.

5. Applicative study

The aim of validating the model is to facilitate process simulations for other applications and demonstrate the interest of this hybrid system on representative case. The configuration chosen for this applicative study consists of the HCTRS producing cold at $T_{ev} = -25\text{ }^{\circ}\text{C}$ from an ambient temperature $T_m = 20\text{ }^{\circ}\text{C}$ (which implies condenser temperature of $T_{cd} = 30\text{ }^{\circ}\text{C}$). Considering NH_3 as working fluid, this temperature difference between cold production and heat rejection would require a too high compression ratio ($P_H/P_L = 7.8$) to implement the MVC system with a single stage only one vapor compressor refrigerator.

5.1. System configuration

The hybrid configuration presented in this case (Fig. 9) is based on a two stages vapor compression refrigerator that uses two compressors in series with an optimized intermediate pressure that maximizes overall COP. The ammonia retired from the thermochemical reactor during decomposition is stored inside the ammonia storage tank for later de-storage during synthesis. This means that, except during periods when only the MVC subsystem operates, the ammonia flow rates \dot{m}_9 and \dot{m}_{10} are different.

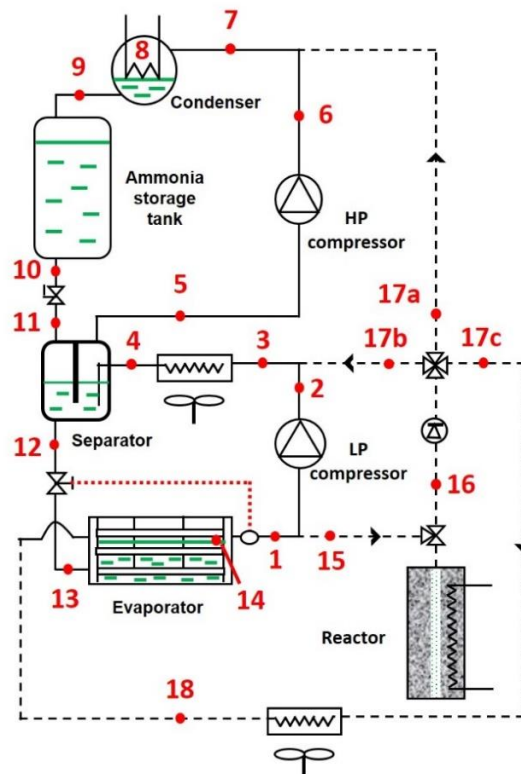


Fig. 9: Flow diagram of the configuration considered for the case study.

394 From the point of view of the TCH reaction, the synthesis is assumed to take place simultaneously with MVC cold
 395 production, and therefore it is carried out at P . As for the decomposition, it has been explained previously that the
 396 operating pressure can be adjusted accordingly to heat source temperature. In this particular configuration, 3 options
 397 are identified (Fig. 9):

- 398 1) TOD at $P_{c,rd} = P_h$;
 399 2) CAD with single-staged compression at $P_{c,rd} = P_m$;
 400 3) CAD with bi-staged compression at $P_{c,rd} = P$.

401 For all results shown in this section (except for some cases of Fig. 14), the TCH decomposition was always
 402 assumed as option 2 (single-stage CAD at $P_{c,rd} = P_m$), and ammonia gas leaving the reactor was assumed to be at
 403 the same temperature as the reaction's equilibrium one at $P_{c,rd}$.

404 Figure 10 shows the process on the ammonia's h-P diagram. The cycle is carried out with total injection, and the
 405 three pressure levels are labelled on the diagram. The three options for decomposition of the TCH reactive are also
 406 displayed. The same type of compressor was chosen for both high-pressure and low-pressure regions: GEA Bock
 407 Open Type Ammonia Compressor, model F14/1366 NH3 [36]. Functions of isentropic efficiency with respect to P_m
 408 were derived for both compressors from data in the technical sheet.

409 The determination of the COP, defined by equation 13, is based on energy and mass balances with some classical
 410 hypotheses as: steady-state running, isenthalpic expansion through throttle valves, temperatures of ammonia near
 411 to ambient temperature after exchange with it ($T_4 = T_{18} = T_{amb} + 5K$; $T_{10} = T_{amb} + 2K$), separator perfectly insulated,
 412 no pressure drops in pipes...

$$413 \quad COP = \frac{\dot{Q}_{ev}}{\dot{W}_{LP} + \dot{W}_{HP}} \quad (13)$$

414 For the MVC subsystem alone this coefficient depends only of the specific enthalpies h_i where the subscript "i"
 415 refers to the point "i" in the figures 9 and 10 (eq. 14):

$$416 \quad COP_{MVC} = \frac{\dot{m}_{LP} \cdot (h_1 - h_{13})}{\dot{m}_{LP} \cdot (h_2 - h_1) + \dot{m}_{HP} \cdot (h_6 - h_5)} = \frac{h_1 - h_{13}}{(h_2 - h_1) + [(h_4 - h_{12}) / (h_5 - h_{11})] \cdot (h_6 - h_5)} \quad (14)$$

417 For the HCTRS this coefficient depends also on mass flows exchanged with the reactor, and this one is different
 418 during the synthesis (eq. 15) or decomposition (eq. 16):

$$419 \quad COP_{HYB,syn} = \frac{[\dot{m}_{LP} + \dot{m}_{rs}(t)] \cdot (h_1 - h_{13})}{\dot{m}_{LP} \cdot (h_2 - h_1) + \dot{m}_{HP} \cdot (h_6 - h_5)} \quad (15)$$

$$420 \quad COP_{HYB,dec} = \frac{\dot{m}_{LP} \cdot (h_1 - h_{13}) - \dot{m}_{rd,17c}(t) \cdot (h_{18} - h_{13})}{\dot{m}_{LP} \cdot (h_2 - h_1) + \dot{m}_{HP} \cdot (h_6 - h_5)} \quad (16)$$

421 with the mass flows deduced from mass balance and energy balance on the separator respectively for the
 422 synthesis phase (eq. 17) and decomposition one (eq. 18):

$$423 \quad \dot{m}_{HP} \cdot (h_{11} - h_5) + \dot{m}_{LP} \cdot (h_4 - h_{12}) + \dot{m}_{rs}(t) \cdot (h_{11} - h_{12}) = 0 \quad (17)$$

$$424 \quad \dot{m}_{HP} \cdot (h_{11} - h_5) + \dot{m}_{LP} \cdot (h_4 - h_{12}) + \dot{m}_{rd,17b}(t) \cdot (h_4 - h_{11}) + \dot{m}_{rd,17c}(t) \cdot (h_{12} - h_{11}) = 0 \quad (18)$$

425 Note that $\dot{m}_{rd,17b}(t)$ and/or $\dot{m}_{rd,17c}(t)$ may be null in equations (16) and (18) according to the option retained for
 426 the CAD.

427 These functions were implemented in the simulation code [37] of the hybrid system, and the $COP = f(P_m)$ diagram
 428 was traced (Fig. 11) for optimization. It was found that $P_m = 5$ bar optimizes COP_{MVC} . It was assumed that the value
 429 of P_m that optimizes COP_{HYB} would be very close to this value, for three reasons. First, the MVC subsystem is
 430 operating during most of the time. Second, the ammonia stream of the TCH subsystem during CAD is consequently
 431 lower than the stream in MVC. Third, optimal P_m for single-stage CAD must prioritize the high-pressure compressor,
 432 same as for MVC alone (Fig. 11).

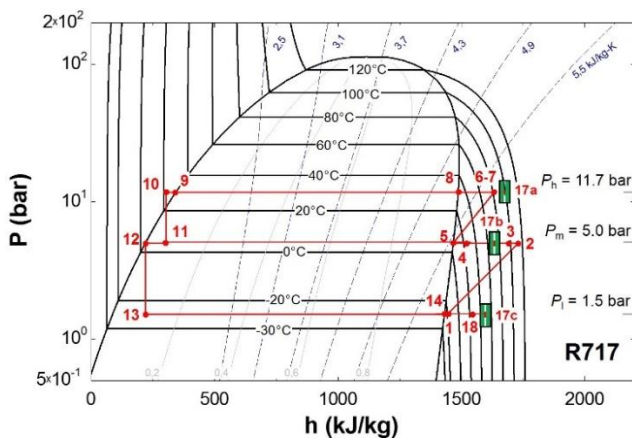


Fig. 10: Hybrid compression-thermochemical deep-freezing cycle represented on the h-P diagram with the configuration that includes bi-staged compression at the intermediate pressure that optimizes global system's COP.

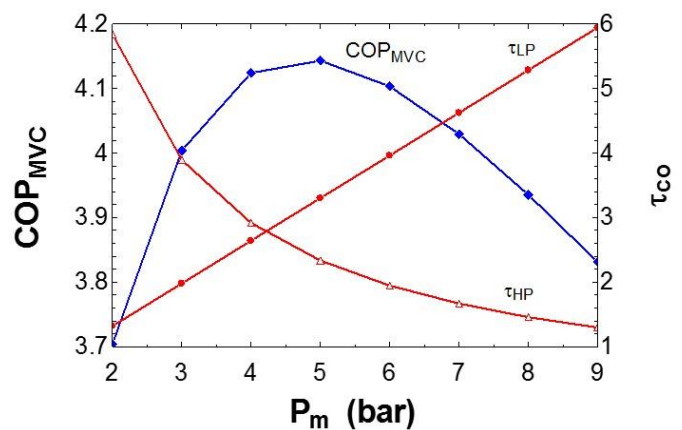


Fig. 11: Global COP optimization of the bi-staged configuration for the case study. Evolution of COP of the MVC subsystem and compression ratio of the low-pressure and high-pressure compressors as a function of intermediate pressure. Optimal intermediate pressure was found at 5 bar by taking into account isentropic efficiency of the two compressors.

433 5.2. Operation scenario

434 Different scenarios are possible. It could be assumed, for instance, that the compressors are driven off-grid by
 435 solar-PV electricity. This approach would result in ammonia storage during the day (because of sun availability) and
 436 cold production at night (to cover the demand by TCH synthesis since compressors cannot work). Different
 437 hypotheses are also applicable for the driving heat: it could be waste heat, or generated by solar thermal collectors,
 438 with interesting consequences on operating modes distribution and performance evaluation.

439 The scenario supposed for this applicative study is a permanent cooling load of 40 kW for food freezing in an
 440 industrial chamber. Both compressors of the hybrid system are driven by on-grid electricity, and the CAD reactor
 441 decomposition is activated with waste heat from another industrial process (therefore, at zero cost). Given the
 442 assumptions of constant demand of cold and unlimited availability of both grid electricity and waste heat for a given
 443 reactor design, the only decision factor for switching between operating modes is electricity price. It is assumed that
 444 the lowest price takes place during the night, while peak prices occur in late evening. Figure 12 represents in “watch
 445 shape” the behavior of the HCTRS in this scenario for one full cycle (24 hours, midnight to midnight).

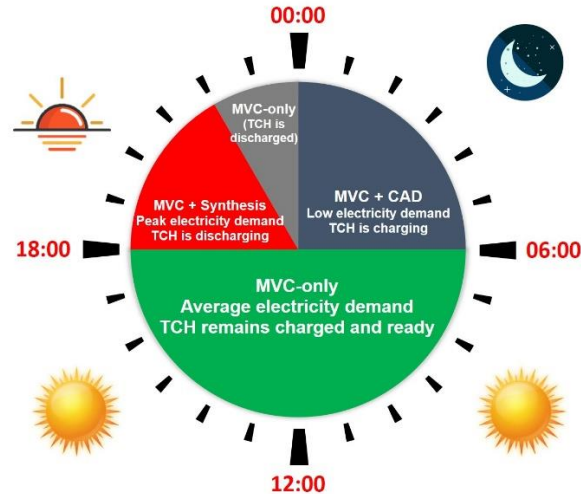


Fig. 12: “Watch-shaped” representation of operating periods of the hybrid compression-thermochemical freezing system in the case study. Global cycles of 24 hours (midnight to midnight) are considered, with a total of four different operating periods throughout the day.

446

447 Three operating modes are identified:

- 448 1) “MVC + CAD” from 00:00 to 06:00, period of lowest electricity price. The whole demand of cold is satisfied
449 by MVC while ammonia from the TCH subsystem is being stored in the ammonia storage tank (in other
450 words, the TCH is charging by means of the endothermic reaction from eq. 1).
- 451 2) “MVC-only” when electricity price is average. The hybrid system proceeds just as an MVC cycle, and the
452 ammonia of TCH reaction remains stored. This mode is assumed to take place between 06:00 and 18:00
453 and between 22:00 and 00:00. These two periods are represented with distinct colors to differentiate
454 between “MVC-only” with TCH fully charged or fully discharged.
- 455 3) “MVC + Synthesis” for the peak demand period of 18:00 – 22:00. A part of the cooling load is satisfied by
456 MVC while the other part is covered by discharging ammonia from the storage tank through TCH
457 synthesis (exothermic reaction from eq. 1), reducing consumption of mechanical power by both
458 compressors, and hence electric consumption.

459 Although each operating period is presented as a block in Fig. 12, their distribution in a more realistic case study
460 may well be scattered throughout the day. For instance, another peak electricity price can occur at morning between
461 06:00 and 08:00. Operation of the HCTRS is still feasible in such cases, because the TCH reaction can be interrupted
462 mid-progress and resumed later, with no penalization on total ammonia production. Nevertheless, as this is a
463 preliminary case study, the simplified approach presented here was considered sufficient.

464 Two reactive salts were considered for this case study: SrCl_2 and CaCl_2 , whose activation temperatures for CAD
465 at $P_{c,dec}$ are suitable for low-grade waste heat utilization (Fig. 3). The calculation procedure combined the dual front
466 quasi-steady reaction model described in Section 3 with a nodal model based on mass and energy balances for
467 global cycle simulation. The calculation process was done in three steps:

- 468 1) For the given constraint temperature of $T_c = T_m = 20$ °C during synthesis phase, adjust reactive
469 composite’s diameter to complete synthesis phase (cold production) within 4 hours (18:00 – 22:00). In
470 this step, the same \tilde{p}_{ENG} and w_{sa} as with experimental implementation of the BaCl_2 are kept. This allows
471 to keep also the same values of $\lambda_0 (= \lambda_1)$, $k_0 (= k_1)$ and $Uw_0 (=Uw_1)$ that were adjusted for model validation.
- 472 2) After adjusting composite’s diameter, adjust T_h to complete CAD at P_c equal to P_m or P_1 , or to complete
473 TOD at P_c equal to P_h , accordingly to the option chosen for the decomposition within 6 hours (00:00 –
474 06:00).

- 3) Obtain $\dot{m}_{NH_3} = f(t)$ for synthesis and CAD or TOD and implement these values in the global simulation to obtain data on cold production and power consumption.

We propose a performance indicator ψ , defined as the COP ratio between the hybrid system and mechanical vapor compression, with COP_{MVC} and COP_{HYB} themselves defined by equations (14) to (16).

The value of this indicator is calculated with two different approaches: for Figs. 13 and 14, it is calculated in terms of power at each time step (and noted $\dot{\psi}$, equation (19)), while for Fig. 15 it is calculated in terms of energy (and noted ψ) by integrating throughout the whole period of either synthesis (ψ_{syn} , eq. (20)), decomposition (ψ_{dec} , eq. (21)), or the overall thermochemical cycle ($\psi_{syn-dec}$, eq. (22)). In these cases, as the cooling energy is the same for each period, the ratio of COP is also equal to the ratio of mechanical energy required by the MVC and HCTRS

$$\dot{\psi}_{\#} = \frac{COP_{HYB,\#}}{COP_{MVC}} = f(t) \quad \{\# = syn, dec\} \quad (19)$$

$$\psi_{syn} = \frac{\int_{18h}^{22h} COP_{HYB,syn} \cdot dt}{COP_{MVC}} = \frac{\int_{18h}^{22h} (\dot{W}_{LP} + \dot{W}_{HP})_{MVC} \cdot dt}{\int_{18h}^{22h} (\dot{W}_{LP} + \dot{W}_{HP})_{HYB,syn} \cdot dt} \quad (20)$$

$$\psi_{dec} = \frac{\int_{0h}^{6h} COP_{HYB,dec} \cdot dt}{COP_{MVC}} = \frac{\int_{0h}^{6h} (\dot{W}_{LP} + \dot{W}_{HP})_{MVC} \cdot dt}{\int_{0h}^{6h} (\dot{W}_{LP} + \dot{W}_{HP})_{HYB,syn} \cdot dt} \quad (21)$$

$$\psi_{syn-dec} = \frac{\int_{18h}^{22h} (\dot{W}_{LP} + \dot{W}_{HP})_{MVC} \cdot dt + \int_{0h}^{6h} (\dot{W}_{LP} + \dot{W}_{HP})_{MVC} \cdot dt}{\int_{18h}^{22h} (\dot{W}_{LP} + \dot{W}_{HP})_{HYB,syn} \cdot dt + \int_{0h}^{6h} (\dot{W}_{LP} + \dot{W}_{HP})_{HYB,syn} \cdot dt} \quad (22)$$

Note that \dot{W}_{MVC} corresponds to the mechanical power consumption of the compressors if all the cooling load was satisfied by MVC exclusively.

On the other hand the part ε of the cooling effect assumed by the TCH subsystem in the hybrid system can be chosen arbitrary (eq. 23) between the two extreme values 0 and 1:

$$\varepsilon = \frac{Q_{ev,TCH,syn}}{Q_{ev,HYB,syn}} \quad (23)$$

5.3. Results

Figure 13 shows results for one full cycle with a dimensioning of the TCH reactor for $\varepsilon = 0.5$ (i.e. to cover 50 % of the cooling load) in the “MVC + Synthesis” period and with P_c equal to P_m during CAD phase. For more clarity, the x-axis includes background color traces to distinguish between operating modes that are identical to those of Figure 12. Values on the right y-axis correspond to total cooling power (blue line) and power consumption from low-pressure

498 compressor (purple continuous line) and high-pressure compressor (purple dashed line). Left y-axis is exclusive for
 499 the ratio between COP of the hybrid system and COP if all cooling load was covered by MVC alone.

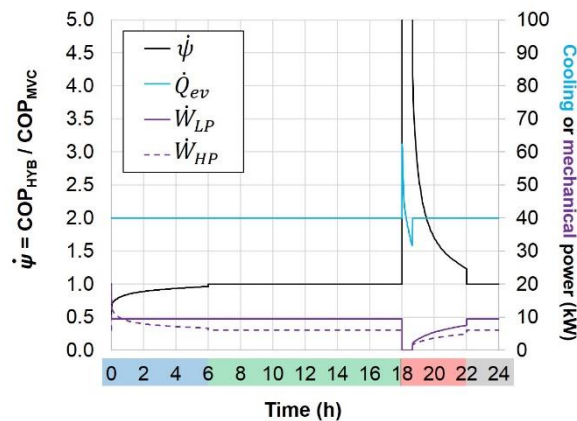


Fig. 13: Evolution of COP ratio calculated in terms of power ($\dot{\psi}$), cooling power and mechanical power consumption of low-pressure and high-pressure compressors of the bi-staged hybrid compression-thermochemical freezing system, for one full cycle (24 hours) at nominal case ($\varepsilon = 0.5$) and $P_{c,dec} = P_m$. Each operating mode is depicted on the x-axis with its corresponding color (see Fig. 12).

500

501 The 06:00 – 18:00 and 22:00 – 24:00 periods can be considered as “regular” periods in this figure: all cooling load
 502 is satisfied by MVC alone, and power consumption from both compressor remains steady. These values serve for
 503 calculation of the COP_{MVC} that is later used for calculation of $\dot{\psi}$. Obviously, in these periods $\text{COP}_{\text{HYB}} = \text{COP}_{\text{MVC}}$, which
 504 means $\dot{\psi} = 1$. As for power consumption, that of the high-pressure compressor is lower than that of the low-pressure
 505 compressor despite the fact that the mass flow is higher. This is coherent with the fact that $P_m = 5$ bar yields lower
 506 values of η_{HP} than of η_{LP} and finally better value of the isentropic efficiency for the high-pressure compressor (see
 507 Fig. 11).

508 The 00:00 – 06:00 period corresponds to “MVC + CAD”. The cooling load remains constant at target value and is
 509 still satisfied by MVC alone, which explains why power consumption from the low-pressure compressor remains the
 510 same as in “MVC-only”. However, power consumption from the high-pressure compressor is higher, in accordance
 511 with CAD at P_m . Since decomposition is carried out at intermediate pressure, only the high-pressure compressor has
 512 increased power consumption. It shows peak consumption at the beginning and decays gradually until the end, and
 513 the final value right before switching to the next mode is very close to power consumption in “regular” operation. This

514 profile is coherent with $\dot{m}_{rd,NH_3} = f(t)$ during decomposition, since the reaction is faster at the beginning (see Fig.
 515 6). This additional power consumption implies ψ lower than unity, and this parameter follows the same curve as \dot{W}_{HP}
 516 but in the opposite sense.

517 The 18:00 – 22:00 period shows three noteworthy traits: 1) Cold production is variable during the first hour, with
 518 a peak of surplus and a peak of shortage; 2) During this same interval, power consumption from both compressors
 519 drops to zero; 3) During this same interval, ψ tends to infinity.

520 The variations of \dot{Q}_{ev} are caused by the variations of $\dot{m}_{rs,NH_3} = f(t)$ in thermochemical synthesis, similarly to CAD.
 521 Congelation in an industrial chamber usually implies big quantities of food: therefore, the strategy chosen in this study
 522 is to let the TCH subsystem produce surplus cold in early synthesis reaction. This surplus cold is stored by the end
 523 product itself in the form of slightly lower temperature. This thermal inertia compensates for the sub-par cold
 524 production in the later stage of synthesis. As soon as the deficit in cold production equals surplus production from
 525 the previous stage, the compressors start working and the remainder of cooling load is supplied by MVC (please
 526 note that at this point the TCH subsystem is still producing cold, as shown by a lower power consumption by the
 527 compressors between 19h and 22h).

528 The fact that both \dot{W}_{LP} and \dot{W}_{HP} drop to zero means that the TCH process is covering all cooling load. The whole
 529 ammonia stream leaving the evaporator enters the reactor directly, instead of flowing to the compressors. This is
 530 synchronized with the surplus/deficit peaks of production. After, power consumption increases gradually as the
 531 synthesis reaction advances, since more and more mass flow rate of ammonia is flowing to the compressors. \dot{W}_{LP}
 532 increases faster than \dot{W}_{HP} because it compresses a slightly larger stream of ammonia. By the end of the operating
 533 period, both power consumptions are close to MVC values, which indicates that the synthesis is close to finishing
 534 and the mass flow rate of ammonia entering the reactor is close to zero.

535 The value of ψ tending to infinity is a logical consequence of power consumption dropping to zero. COP_{HYB} is
 536 defined as the ratio of cold production to power consumption, so the denominator reaches 0. Right when compressors
 537 start working again, this parameter ψ decreases back, but always maintaining itself at a value higher than 1. The
 538 authors wish to point out that the definition of COP_{HYB} in these calculations does not include the heat of reaction
 539 during decomposition, since it is assumed to be waste heat with no cost. Regardless, this figure shows the potential
 540 interest of the hybrid system in reducing total power consumption.

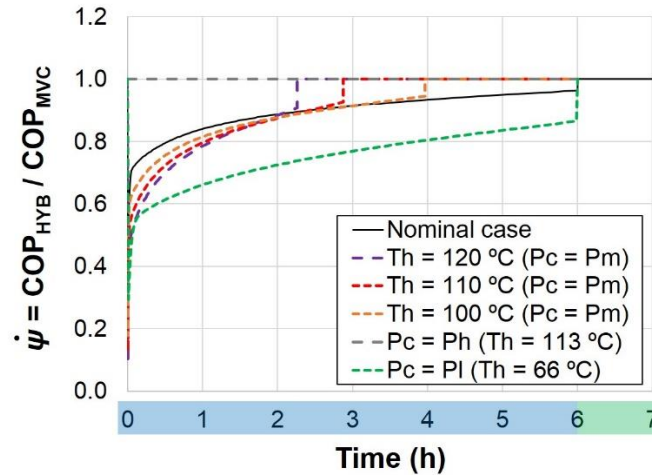


Fig. 14: Effect of constraint pressure and temperature of the heat source on system's performance during decomposition phase.

541

542 Figure 14 shows a sensitivity analysis on the influence of other values of T_h or P_c during decomposition reaction.
 543 This figure can be regarded as a zoomed view of the first 7 hours of operation of Fig. 13, including nominal case
 544 (with the same black line as in Fig. 13) and some alternate cases. Three of these alternate cases involve increasing
 545 T_h at same $P_c (= P_m)$: as a consequence the decomposition finishes earlier than in nominal case, but the drop in $\dot{\psi}$ is
 546 bigger because peak power consumption is higher. The fourth alternate case involves TOD ($P_c = P_h$) instead of CAD
 547 ($P_c = P_m$ or $P_c = P_l$), resulting in a constant $\dot{\psi}_{dec} = 1$ because Q_{rd} is assumed no-cost and therefore not taken into
 548 account for COP_{HYB} definition. Nevertheless, this case requires higher T_h than nominal, which can make finding an
 549 appropriate waste heat source more difficult. The fifth and final alternate case involves CAD at P_c equal to P_l instead
 550 of P_m : this case requires lower T_h than nominal, making it easier to find waste heat sources. The downside is a clearly
 551 higher power consumption because both compressors proceed during decomposition, while in CAD at intermediate
 552 pressure only the high-pressure compressor proceeds. This figure is interesting for analyzing the potential flexibility
 553 of this system in adapting to different operating schedules and heat source availability. Main results of the nominal
 554 case are shown in Table 3. Some differences can be seen between the process with SrCl_2 or with CaCl_2 . For instance,
 555 CaCl_2 shows lower activation temperatures at the same operating pressures. On the other hand, reactor volume is
 556 smaller with SrCl_2 thanks to its higher energy density.

557

Table 3. Operating conditions and performance figures of the HCTRS in the applicative study at nominal case ($\varepsilon = 0.5$ and $P_{c,rd} = P_m$)

Parameter \ Salt	SrCl ₂	CaCl ₂
Δh_r^0 [kJ · kmol-NH ₃ ⁻¹]	41432	41013
Δs_r^0 [kJ · kmol-NH ₃ ⁻¹ · K ⁻¹]	132.9	134.4
M_{sa} [kg/kmol]	158.53	110.98
\tilde{p}_{ENG} [kg/m ³]	100	
w_{sa}	0.71	
Dec [kWh/m ³]	125	101
m_{salt} [kg]	313	384
m_{ENG} [kg]	127	156
V_r [m ³]	1.28	1.57
$T_{h,min}$ [°C] with $P_c = P_h$	112.7	99.8
$T_{h,min}$ [°C] with $P_c = P_m$	91.0	78.9
$T_{h,min}$ [°C] with $P_c = P_l$	66.3	54.4
ψ_{syn}	2.056	2.066
ψ_{dec}	0.892	0.892
$Q_{ev,MVC}$ [kWh]	80.0	
$Q_{ev,TCH}$ [kWh]	80.0	
$W_{LP,syn}$ [kWh]	17.8	17.7
$W_{HP,syn}$ [kWh]	12.2	12.1
$W_{LP,dec}$ [kWh]	56.3	56.3
$W_{HP,dec}$ [kWh]	47.3	47.3
Q_{rd} [kWh]	158.9	157.4

558

559 Figure 15 shows an analysis of main performance figures in this case study, for several scenarios between $\varepsilon = 0$
560 (no TCH subsystem at all) and $\varepsilon = 1$ (all cooling load is provided by TCH during synthesis period) but always (except
561 for $\varepsilon = 0$) with P_c equal to P_m during the CAD periods. The case $\varepsilon = 0.5$ corresponds to the nominal case. In this figure
562 any indicator with the “syn” subscript, as well as cold production by MVC and TCH, correspond to integration within
563 the whole duration of the “Synthesis” operating mode (18:00 to 22:00). Indicators with the “dec” subscript are
564 calculated by integration within the whole duration of the “MVC + CAD” operating mode. And finally $\psi_{syn-dec}$
565 coefficient is calculated by integration within the overall duration of the thermochemical cycle including the synthesis
566 and decomposition reactions (eq. 20 to 22). In the y-axes, magnitudes shown above the zero point are related to the

567 system's useful effect: cold production by MVC and TCH shown as bars (left y-axis), and ψ in synthesis,
 568 decomposition and overall thermochemical cycle shown as lines (right y-axis). For more clarity a change in scale for
 569 ψ_{syn} is operated for the values of ε upper to the nominal case ($\varepsilon > 0.5$). On the other hand, magnitudes shown below
 570 the zero point are related to the system's "inputs": compressors' power consumption during synthesis and
 571 decomposition (with yellow and grey bars, left y-axis), heat of decomposition reaction (red bars, left y-axis), and
 572 volume of reactive composite (blue line, right y-axis).

573 At $\varepsilon = 0$, the whole cooling load (40 kW during 4 hours, i.e. 160 kWh) is satisfied by MVC only, which explains the
 574 absence of $Q_{ev,TCH}$ and Q_{rd} . Also, both ψ_{dec} and ψ_{syn} equal 1 and V_r equals 0, because there is no TCH subsystem at
 575 all. At the other extreme case ($\varepsilon = 1$) the demand in peak period is entirely covered by the TCH process, so there is
 576 no MVC cold production nor compression power consumption during synthesis and ψ_{syn} goes to infinity. As ε
 577 increases, the TCH process gains more and more presence in the hybrid system and results reflect this tendency.
 578 The cooling load is more covered by the thermochemical reaction and less by MVC, and accordingly, mechanical
 579 power consumption during synthesis phases becomes lower and lower (yellow bars in Fig. 15). On the other hand,
 580 mechanical power consumption in CAD increases gradually (grey bars in Fig. 15), as there is more and more
 581 ammonia vapor from the reaction that has to be compressed, so the ψ_{dec} decreases, but moderately until the value
 582 of 0.82 at ε equal to 1. Finally for the overall thermochemical cycle the gain of the COP by the hybrid system is
 583 positive; $\psi_{syn-dec}$ evolves between 1 and 1.4 for ε varying from 0 to 1. This tendency of $\psi_{syn-dec}$ in the figure 15
 584 corresponds also to the ratio between the total cold energy produced (sum of purple and blue bars, i.e. 160 kWh)
 585 and the total required mechanical power (sum of yellow and grey bars). Of course this evolution, although positive,
 586 is not very important, but we must not forget that the main objective of this hybrid HCTRS, in this case of application,
 587 was to reduce particularly the mechanical power absorbed during the hours of peak for electric consumption (i.e.
 588 between 18h and 22h); this goal is largely achieved with ψ_{syn} values of about 2 up to 15.4 for respective ε values of
 589 0.5 and 0.9.

590 Obviously the higher the ε value the more the volume of the reactor and the thermal power to be supplied to it
 591 during the decomposition phases as well. For example (Fig. 15), at ε equal to 0.8, the volume of the reactive
 592 composite is 2m³ and the heat required in decomposition is 250 kWh at 91 °C, again for a cooling production of 160
 593 kWh at -25 °C.

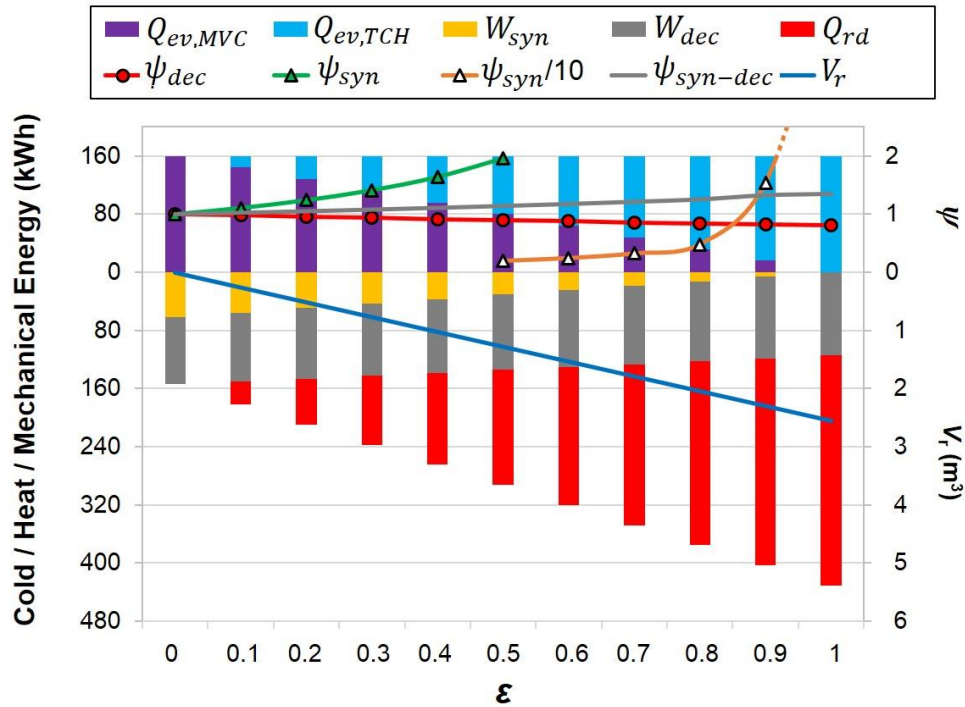


Fig. 15: Effect of target share of cold for the thermochemical subsystem (ϵ) on several variables. In synthesis phase: COP ratio (ψ_{syn} and $\psi_{syn}/10$ for $\epsilon \geq 0.5$) and total cold produced (in kWh) by both subsystems. In decomposition phase: COP ratio (ψ_{dec}), total consumption (in kWh) of mechanical energy by the two compressors (low-pressure and high-pressure), and total heat consumption (in kWh) by the thermochemical reactor (at $T_h = 91^\circ\text{C}$). For overall thermochemical cycle: total volume (in m^3) of reactive composite and global COP ratio $\psi_{syn-dec}$.

594 The choice of an optimal ϵ then derives from the relative importance attributed to the reduction of the electrical
 595 consumption and the corresponding increase of the thermal power required for the decomposition phases. The
 596 relative cost of the two energies (electrical and thermal) should be taken into account both for the investment of the
 597 hybrid system (globally proportional to ϵ) and for its operation. This is outside the scope of this 1st study.

598 **6. Conclusions and perspectives**

599 The hybrid compression / thermochemical refrigeration system (HCTRS) presented in this paper is expected to
 600 valorize low-grade waste heat thanks to the connection between compressor and thermochemical reaction. This
 601 hybrid system has three characteristic operating modes, and each one of them allows cold production by mechanical
 602 vapor compression while either storing or de-storing refrigerant simultaneously. One of these modes allows additional
 603 cold production with no additional power consumption thanks to the thermochemical synthesis reaction. The second
 604 mode allows storing refrigerant with no additional power consumption, by using a heat source below 120°C . The

605 third mode connects the compressor and the thermochemical reactor to drop reactor pressure during the refrigerant
606 storage phase, with the idea of reducing heat source temperature.

607 Our experiences proved this reduction in heat source temperature. Thanks to the compressor-reactor coupling,
608 an experiment with the $\text{BaCl}_2/\text{NH}_3$ reaction was possible with a reactor pressure as low as 0.5 bar (condenser
609 pressure being kept at 3.5 bar because one small compressor alone was used). At this pressure, process activation
610 was possible with a heat source at ambient temperature (20 °C). Without assisting the decomposition reaction with
611 the compressor, reactor pressure would have been 3.5 bar. With this pressure and respecting the same equilibrium
612 drop, process activation would have required a source heat temperature of 55 °C, i.e. 35K above.

613 To allow further simulations of this system, a quasi-steady simulation model was validated from experimental
614 data, through adjustment of the thermal conductivity and the permeability of the reactive composite, as well as the
615 global heat transfer coefficient between reactive composite and heat transfer fluid from the reactor's thermal jacket,
616 respectively at the values $1.4 \text{ W}\cdot\text{m}^{-1}\cdot\text{K}^{-1}$, 10^{-14} m^2 and $170 \text{ W}\cdot\text{m}^{-2}\cdot\text{K}^{-1}$. The three values are within the reasonable
617 range, based on literature data on thermochemical systems. After parameter adjustment, the quasi-steady simulation
618 model predicted the $X-t$ curves of reaction accurately enough in synthesis, thermally-only activated decomposition
619 and compression-assisted decomposition. In the particular case of compression-assisted decomposition, which is
620 the most characteristic mode of this system, mass transfer limitations were not negligible, given the low operating
621 pressures.

622 The validated quasi-steady simulation model allowed a first law assessment of system performance in a
623 preliminary and nevertheless realistic case study. The scenario was the HCTRS operating in cycles of 24 hours to
624 produce 40 kW cold at -25 °C for a food conservation industrial chamber, by running a bi-stage MVC cycle with full
625 injection that implies two compressors in series and with a condenser temperature of 30 °C. From the point of view
626 of electricity source, the compressors were supposed grid-driven and the HCTRS was storing refrigerant in off-peak
627 electric demand periods for later discharge during peak periods. Results indicated that the hybrid can reach, during
628 ammonia de-storage phase, many times higher COP than a mechanical vapor compression refrigeration cycle,
629 depending on the share of cold production (quantified by the ε parameter) that is covered by the TCH process.

630 The study also considered an alternate case in which compression-assisted decomposition is carried out at a
631 pressure of 1.5 bar, which implies equilibrium temperatures as low as 20 °C, 35 °C and 45 °C for reactions with BaCl_2 ,
632 CaCl_2 and SrCl_2 , respectively. In the particular case of BaCl_2 , this bi-staged compression can eventually allow
633 process activation with heat at ambient temperature. Our experience D3 proved this activation at ambient

634 temperature, although condenser pressure was pretty low (3.5 bar) because the experimental bench had just one
635 compression stage. Thus, an experimental study with two compressors in series is definitely an interesting prospect,
636 now that the single-stage compression-assisted decomposition has been experimentally proven.

637 Another interesting question waiting for an answer is whether or not the HCTRS competes economically with
638 state-of-the-art solutions such as electric batteries or phase change materials. Implementing the thermochemical
639 process to a compression refrigeration cycle is probably more expensive than these two options, but as long as a
640 source of free waste heat can be utilized, it can compensate in the long term. After all, both electricity stored by
641 batteries and cold stored by phase change materials come from a surplus consumption of electricity at some point.
642 The HCTRS proceeds the same way, but as long as source heat is free and operating pressure during decomposition
643 can be adjusted, higher heat source temperatures result in lower power consumption by the compressor, and
644 therefore, potentially much higher COP [28]. Moreover, thermochemical processes should have less inertia than
645 batteries in the discharge phase, since the stored material is liquid refrigerant, and can be preferable to phase change
646 materials if no modifications should be made at the cold delivery unit. In addition, the liquid refrigerant is stored at
647 ambient temperature, with no concerns about thermal isolation, which is an advantage in front of other options such
648 as sensible thermal storage. An appropriate economic assessment may eventually answer the question about
649 competitiveness.

650 As final statement the authors of this paper believe that, although the Compression/Thermochemical System may
651 seem less promising than its 'twin', i.e. the Expansion/Thermochemical System (electricity and heat inputs for cold
652 production versus heat input for electricity and cold production), its compression-assisted reduction of activation
653 temperature is a powerful enough tool to find a niche.

654 **Acknowledgement**

655 The authors are thankful for their financial support to the French " Investments for the future " program managed
656 by the National Agency for Research under contract ANR-10-LABX-22-01 (Labex SOLSTICE), the Spanish Ministry
657 of Economy and Competitiveness (MINECO) and FEDER/UE (Project DPI2015-71306-R).

658 **References**

- 659 [1] Climate Change 2001. The Scientific Basis. Third Assessment Report. UN Intergovernmental Panel on
660 Climate Change. Cambridge University Press, ISBN 0521 01495 6. n.d.
- 661 [2] Ademe: Le froid alimentaire commercial. Agence de l'Environnement et de la Maîtrise de l'Énergie.

- 662 www.ademe.fr [Last updated: 17/12/2014] n.d.
- 663 [3] Kim DS, Infante Ferreira CA. Solar refrigeration options - a state-of-the-art review. *Int J Refrig* 2008;31:3–
664 15. doi:10.1016/j.ijrefrig.2007.07.011.
- 665 [4] Cao S, Hasan A, Sirén K. On-site energy matching indices for buildings with energy conversion, storage
666 and hybrid grid connections. *Energy Build* 2013;64:423–38. doi:10.1016/j.enbuild.2013.05.030.
- 667 [5] Fitó J, Mauran S, Stitou D, Mazet N, Coronas A. New solar hybrid absorption / thermochemical refrigeration
668 cycle. *ECOS 2015 - 28th Int. Conf. Effic. Cost, Optim. Simul. Environ. Impact Energy Syst.*, 2015.
- 669 [6] Zeyghami M, Goswami DY, Stefanakos E. A review of solar thermo-mechanical refrigeration and cooling
670 methods. *Renew Sustain Energy Rev* 2015;51:1428–45. doi:10.1016/j.rser.2015.07.011.
- 671 [7] El-Bahloul AAM, Ali AHH, Ookawara S. Performance and Sizing of Solar Driven dc Motor Vapor
672 Compression Refrigerator with Thermal Storage in Hot Arid Remote Areas. *Energy Procedia* 2015;70:634–
673 43. doi:10.1016/j.egypro.2015.02.171.
- 674 [8] Xu Y, Li M, Luo X, Ma X, Wang Y, Li G, et al. Experimental investigation of solar photovoltaic operated ice
675 thermal storage air-conditioning system. *Int J Refrig* 2018;86:258–72. doi:10.1016/j.ijrefrig.2017.11.035.
- 676 [9] Bilgili M. Hourly simulation and performance of solar electric-vapor compression refrigeration system. *Sol*
677 *Energy* 2011;85:2720–31. doi:10.1016/j.solener.2011.08.013.
- 678 [10] Mette B, Kerskes H, Drück H. Concepts of long-term thermochemical energy storage for solar thermal
679 applications – Selected examples. *Energy Procedia* 2012;30:321–30. doi:10.1016/j.egypro.2012.11.038.
- 680 [11] Stitou D, Mazet N, Mauran S. Experimental investigation of a solid/gas thermochemical storage process for
681 solar air-conditioning. *Energy* 2012;41:261–70. doi:10.1016/j.energy.2011.07.029.
- 682 [12] Mauran S, Lahmidi H, Goetz V. Solar heating and cooling by a thermochemical process. First experiments
683 of a prototype storing 60 kW h by a solid/gas reaction. *Sol Energy* 2008;82:623–36.
684 doi:10.1016/j.solener.2008.01.002.
- 685 [13] Michel B, Neveu P, Mazet N. Comparison of closed and open thermochemical processes , for long-term
686 thermal energy storage applications. *Energy* 2014;72:702–16. doi:10.1016/j.energy.2014.05.097.
- 687 [14] Le Pierrès N, Stitou D, Mazet N. New deep-freezing process using renewable low-grade heat : From the
688 conceptual design to experimental results. *Energy* 2007;32:600–8. doi:10.1016/j.energy.2006.07.024.

- 689 [15] Neveu P, Castaing-Lasvignottes J. Solid-gas chemical heat pumps: Field of application and performance of
690 the internal heat of reaction recovery process. *Heat Recover Syst CHP* 1993;13:233–51.
- 691 [16] Li TX, Wu S, Yan T, Xu JX, Wang RZ. A novel solid-gas thermochemical multilevel sorption thermal battery
692 for cascaded solar thermal energy storage. *Appl Energy* 2016;161:1–10.
693 doi:10.1016/j.apenergy.2015.09.084.
- 694 [17] Wu S, Li TX, Yan T, Wang RZ. Experimental investigation on a novel solid-gas thermochemical sorption
695 heat transformer for energy upgrade with a large temperature lift. *Energy Convers Manag* 2017;148:330–8.
696 doi:10.1016/j.enconman.2017.05.041.
- 697 [18] Jiang L, Wang L, Wang R, Zhu F, Lu Y, Roskilly AP. Experimental investigation on an innovative resorption
698 system for energy storage and upgrade. *Energy Convers Manag* 2017;138:651–8.
699 doi:10.1016/j.enconman.2017.02.014.
- 700 [19] Anyanwu EE. Review of solid adsorption solar refrigeration II: An overview of the principles and theory.
701 *Energy Convers Manag* 2004;45:1279–95. doi:10.1016/j.enconman.2003.08.003.
- 702 [20] Bao HS, Wang RZ, Wang LW. A resorption refrigerator driven by low grade thermal energy. *Energy*
703 *Convers Manag* 2011;52:2339–44. doi:10.1016/j.enconman.2010.12.045.
- 704 [21] Mähr C. *Vergessene Erfindungen - Warum fährt die Natronlok nicht mehr?* DuMont Literatur und Kunst
705 Verlag; 2003.
- 706 [22] Jahnke A, Ziegler F, Karow M. Re-evaluation of the Honigmann-process: thermo-chemical heat store for the
707 supply of electricity and refrigeration. *Proc Heat ...* 2009.
- 708 [23] Jahnke A, Strenge L, Fleßner C, Wolf N, Jungnickel T, Ziegler F. First cycle simulations of the honigmann
709 process with LiBr/H₂O and NaOH/H₂O as working fluid pairs as a thermochemical energy storage. *Int J*
710 *Low-Carbon Technol* 2013;8:55–61. doi:10.1093/ijlct/ctt022.
- 711 [24] Bao H, Ma Z, Roskilly AP. Integrated chemisorption cycles for ultra-low grade heat recovery and thermo-
712 electric energy storage and exploitation. *Appl Energy* 2016;164:228–36.
713 doi:10.1016/j.apenergy.2015.11.052.
- 714 [25] Bao H, Ma Z, Roskilly AP. A chemisorption power generation cycle with multi-stage expansion driven by low
715 grade heat. *Energy Convers Manag* 2017;150:956–65. doi:10.1016/j.enconman.2017.07.032.
- 716 [26] Lu Y, Bao H, Yuan Y, Wang Y, Wang L, Roskilly AP. Optimisation of a novel resorption cogeneration using

- 717 mass and heat recovery. *Energy Procedia* 2014;61:1103–6. doi:10.1016/j.egypro.2014.11.1032.
- 718 [27] Lu Y, Wang Y, Bao H, Yuan Y, Wang L, Roskilly AP. Analysis of an optimal resorption cogeneration using
719 mass and heat recovery processes. *Appl Energy* 2015;160:892–901. doi:10.1016/j.apenergy.2015.01.138.
- 720 [28] Ferrucci F, Stitou D, Ortega P, Lucas F. Mechanical compressor-driven thermochemical storage for cooling
721 applications in tropical insular regions. Concept and efficiency analysis. *Appl Energy* 2018;219:240–55.
722 doi:10.1016/j.apenergy.2018.03.049.
- 723 [29] Vasta S, Palomba V, La Rosa D, Mittelbach W. Adsorption-compression cascade cycles: An experimental
724 study. *Energy Convers Manag* 2018;156:365–75. doi:10.1016/j.enconman.2017.11.061.
- 725 [30] Fitó J. Solar-driven hybrid refrigeration systems based on thermochemical processes. Doctoral Thesis.
726 Universitat Rovira i Virgili, Tarragona, Spain, 2017.
- 727 [31] Touzain P. Thermodynamic values of ammonia-salts reactions for chemical sorption heat pumps. *Proc. Int.*
728 *Sorption Heat Pump Conf.*, München, Germany: 1999, p. 225–36.
- 729 [32] Hui-Bo L, Mazet N, Coudeville O, Mauran S. Comparison of a general model with a simplified approach for
730 the transformation of solid-gas media used in chemical heat transformers. *Chem Eng Sci* 1997;52:311–27.
731 doi:10.1016/S0009-2509(96)00407-1.
- 732 [33] Fitó J, Mauran S, Stitou D, Mazet N, Coronas A. Solar-driven hybrid absorption-thermochemical
733 refrigeration systems: Performance estimation. *Refrig. Sci. Technol.*, 2016. doi:10.18462/iir.gl.2016.1063.
- 734 [34] Lahmidi H, Mauran S, Goetz V. Definition, test and simulation of a thermochemical storage process adapted
735 to solar thermal systems. *Sol Energy* 2006;80:883–93. doi:10.1016/j.solener.2005.01.014.
- 736 [35] Mauran S, Prades P HF. Heat and mass transfer in consolidated reacting beds for thermochemical systems.
737 *Heat Recover Syst CHP* 1993;13:315–9.
- 738 [36] GEA. GEA Open Type Compressors F: The full range of open type compressors and units. 2015.
739 www.gea.com [Visited on June 2018] n.d.
- 740 [37] Klein SA, Alvarado F. *Engineering Equation Solver, Version 10.346. F-Chart software*, Middleton. 2005.
- 741